The Pennsylvania State University
The Graduate School
College of Earth and Mineral Sciences

NUMERICAL MODELING OF LASER-SILICON INTERACTIONS DURING FORMATION OF SELECTIVE EMITTERS

A Thesis in
Materials Science and Engineering
by
Jared J. Blecher

Submitted in Partial Fulfillment
of the Requirements
for the Degree of

Master of Science

May 2012

The thesis of Jared J. Blecher was reviewed and approved* by the following:

Todd A. Palmer
Assistant Professor of Materials Science and Engineering
Thesis Co-Advisor

Tarasankar DebRoy
Professor of Materials Science and Engineering
Thesis Co-Advisor

Suzanne Mohney
Professor of Materials Science and Engineering

Joan M. Redwing
Professor of Materials Science and Engineering
Chair of Intercollege Graduate Degree Program in Materials Science and Engineering

*Signatures are on file in the Graduate School

Abstract

The formation of highly doped selective emitters improves the efficiency of silicon-based solar cells by lowering the contact resistance at the interface between the silicon front surface and the metal contacts. The use of laser doping in which a laser locally melts the silicon substrate and rapidly incorporates the dopant into the silicon can provide faster processing speeds, lower energy inputs, and higher diffusion rates than other methods of forming selective emitters. A mathematical model, which solves for the temperature, velocity, and dopant concentration fields, is used to investigate the characteristics of the molten region during laser doping with a continuous-wave green laser (λ = 532 nm) moving over the sample at speeds up to 8 m/s and laser output powers ranging from 5 to 20 W. The calculated liquid pool widths and dopant distribution profiles are validated with published experimental results. The effects of fluid flow and diffusive movement on the final shape of the dopant distribution profiles are discussed, and figures are provided to illustrate each effect. Process maps are produced to illustrate how the size of the molten pool dimensions, the average dopant concentration, the relative shape of the dopant distribution, and silicon sheet resistance are impacted by the combination of power and scan speed. The molten pool depth and width are important in determining the diffusion profile and the front-side contact width during plating.

High power solid state fiber and disk lasers combine faster processing speeds, deeper weld penetrations, and lower levels of work piece distortion. Both transmissive optics and reflective optics systems are commonly used. When using transmissive optics at high laser powers and prolonged periods of operation, changes in the focal length and beam diameter have been observed, and these changes adversely affect consistency of the processed materials. In this study, the properties of beams delivered using both transmissive and reflective optics systems from the exit of the process fiber through the final focusing optics have been characterized using commercial diagnostic tools. In the transmissive optics system, changes of nearly 8 mm in focal length have been measured with a 500 mm focal optic at 12 kW output power over several minutes of continuous operation. At powers above 4 kW, damage to the anti-reflective coating on a transmissive collimator resulted in a doubling in the beam diameter at the original focal position when using a 200 mm focal optic and a quadrupling of the beam diameter with a 500 mm focal optic. On the other hand, the performance of the reflective optics was not impacted by either increases in power or time at powers up to 12 kW during prolonged laser operation.

Table of Contents

List of Figures

List of Tables

Acknowledgements

My gratitude goes to BP Solar for funding my research efforts. I would like to thank my thesis advisors, Professor DebRoy and Professor Palmer, for their help and guidance during my research. I would also like to thank my family and friends who have supported me during my studies at Penn State.

Chapter 1: Introduction

Background and Motivation

Laser Diagnostics of High Power Lasers

The output power of 1 μm wavelength solid state lasers has increased significantly in recent years, and systems capable of up to 50 kW in output power are now commercially available [1]. In addition, these lasers have a more compact footprint and much higher wall plug efficiencies than previous conventional lasers. By utilizing fiber optic delivery of the laser light, these systems also provide significant flexibility to the end user in terms of automation and the more efficient use of available factory floor space. With these many advantages, high power fiber and disk lasers are gaining in acceptance among manufacturers, particularly in the shipbuilding and automotive industries, and show great promise for deep penetration welding and high rate deposition processes.

It is unclear, though, what the impact that these high laser power densities will have on the transmissive and reflective optics systems currently in common use. Transmissive optics are fabricated from a transparent glass or ceramic, such as fused silica or CaF_2 [2], and use the refractive index of the lens material and the lens curvature to focus the beam. Cooling of the individual lenses in these optics systems is usually performed using circumferentially flowing water mounted in the individual optics supports. The advantages of these optics systems include low weight, ease of use, and ability to change optics in the same processing head. Reflective optics, on the other hand, use highly polished metal, such as copper, with a precise curved surface that directs and focuses the beam to the workpiece. Each optic surface acts as a mirror to manipulate the laser light as it passes through the optics system. These mirrors are water cooled just below the reflective surface, which when combined with the high thermal conductivity of the metal, leads to uniform cooling of the optics surface.

An important consideration in evaluating laser optics systems is their ability to operate effectively at both high powers and long durations without compromising the laser system performance. Changes observed in the weld or deposition geometries would be indicative of instabilities in the optics systems. When using transmissive optics at high laser powers, variations in the beam properties during continuous laser operation have been observed [3,4], resulting in unexpected changes in weld cross section size and shape. For example, Figure 1

shows three autogenous laser weld cross sections made at sharp focus and an output power of 12 kW with a 200 mm focus transmissive collimator and a 200 mm focal length transmissive focusing optic in 12.5 mm thick steel samples over a period of 90 seconds. The differences in the weld cross section profiles are particularly pronounced after 60 and 90 seconds of operation, as the weld depth fluctuates and the profile changes.

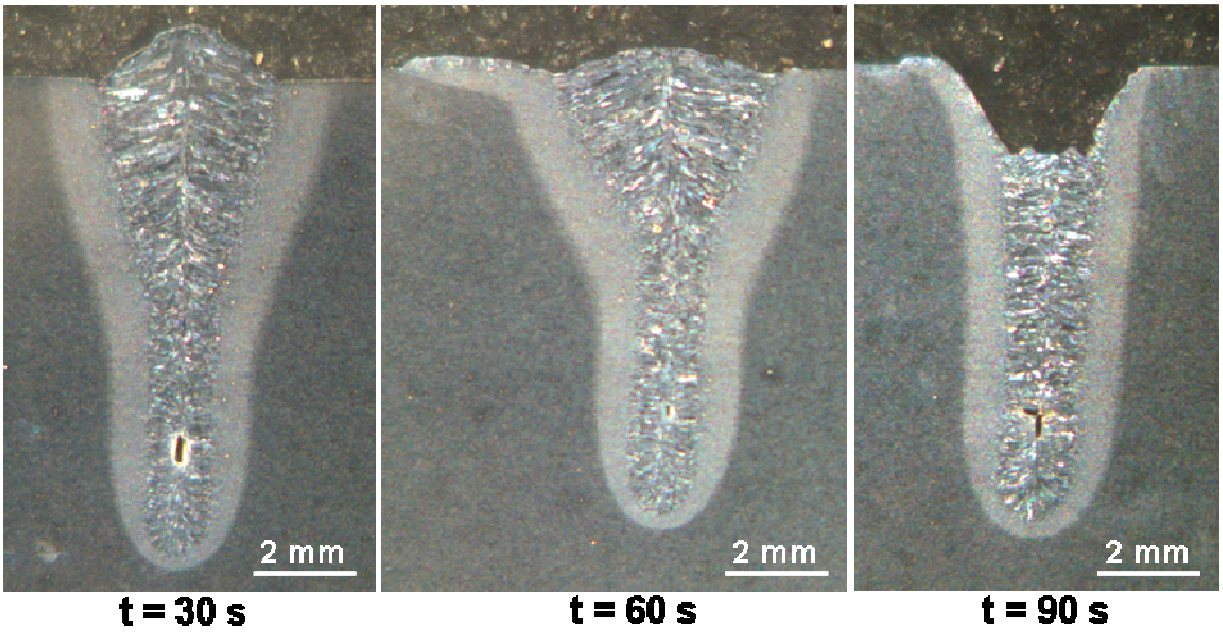

(a) (b) (c)

Figure 1(a-c). Micrographs showing weld cross sections obtained at times of (a) 30 seconds, (b) 60 seconds, and (c) 90 seconds. These welds were made at focus with a 200 mm focal length transmissive optic and 12 kW of output power.

Other researchers have investigated the effects of high power laser beams on transmissive optical elements. Klein [5] determined from the mechanical strength, thermal properties, and optical properties of laser window materials their ability to withstand high incident intensities without causing distortions in the laser beam. This research led to recommendations on the best edge thickness and material for the window, which separates the laser resonator and the rest of the optical system. Reitemeyer et al. [3] examined the individual effects of a transmissive collimator and focus optic on the effective focal length of the beam produced by an 8 kW continuous wave multimode fiber laser. Decreases in focal length of more than 3.1 mm, or 84% of the optics Rayleigh length, were observed and attributed to thermal lensing, which was taken

as increased curvature of the lenses and the changes in the refractive index (dn/dT) with each mechanism having the same impact. Another research group [6] used a novel indirect measurement technique to characterize the focus shift of a transmissive optic system at up to 4 kW of laser output power and observed a 0.5 mm decrease in effective focal length of the optics system. A reflective optic head has been investigated [4] as a means of mitigating thermal lensing effects, and results showed considerable increased beam stability at powers up to 16 kW.

When using transmissive optics, changes in the beam properties are typically attributed to thermal lensing, [5-7] which is generally believed to be caused by thermal gradients that develop across the optics. Since the optic components are made from a glass or ceramic material, the low thermal conductivity of the material does not allow the energy to be rapidly dissipated through heat conduction. In order to mitigate any potential heating issue, the lenses are circumferentially water cooled. However, temperature gradients can form across the lens when operating at high laser powers as a result of uneven cooling. The resulting temperature increase increases the curvature of the lens and the refractive index, thus decreasing the focal length of the optics.

Changes in the focal length of the optics can also be attributed to changes in the refractive index of the optics materials with temperature. The refractive index of a material (n) is equal to the square root of the product of the permeability (μ), which is typically equal to one for optical materials, and the dielectric constant (ε). The refractive index is temperature dependent [8] and is expressed as a function of the thermo-optic coefficient (dn/dT), with units of $°C^{-1}$ and having either a positive or negative sign. In the case of fused silica, the thermo-optic coefficient is positive and not constant [9], which implies that with any significant heating of the material, the refractive index will increase, also resulting in a shorter focus length of the system.

Beam diagnostic tools allow beam characteristics to be investigated in greater detail and determine the magnitude of these changes in beam properties. There are several ways to measure the beam intensity distribution, [10-20] ranging from inexpensive burn paper for characterizing the beam shape to commercial tools that provide a more comprehensive analysis of the beam shape, width, and power density distribution (PDD). These commercially available tools include direct and indirect methods for measuring the PDD. Indirect diagnostic tools attenuate the beam in some fashion before rapidly recording the intensity distribution using a CCD or CMOS camera. Even though these cameras provide very rapid data collection, they can

only handle a few watts of laser power, and the beam is usually directed through a highly reflective window to drastically reduce the laser power incident on the camera.

Direct tools are able to record the entire beam profile without the need to attenuate the beam. Several commercially available direct diagnostic instruments, such as the Primes® Focus Monitor and Beam Monitor, are spinning probe diagnostic tools which use a small aperture that moves through the beam profile and collects the intensity value at discrete positions. Because the probe is manufactured from a reflective metal and moves quickly through the beam path, these instruments can sustain high incident laser powers without the need for attenuation of the beam.

The ability of the optics to produce a stable and consistent beam is an important quality control issue and a key characteristic for laser operators and process engineers to consider when evaluating the industrial use of these high power systems. In this study, the beams produced by selected transmissive and reflective optics systems operating at laser powers up to 12 kW over several minutes of operation have been characterized using commercially available diagnostic tools. Their performance was then compared to reflective optics systems. By combining these results with the modeling of optics performance using ray tracing tools, the origins of these changes in optics performance are evaluated and recommendations for the selection of appropriate optics systems are provided, so that process engineers and laser operators can make informed decisions concerning the selection of the appropriate optics systems for high power laser operations.

Laser Processing of Photovoltaics

Photovoltaic electricity generation is a major growth industry with expected world-wide installed power generation expected to increase fivefold from now to 2020 [21]. In a typical solar cell, a uniform n-type emitter is diffused into the front surface. Figure 2 shows a schematic diagram of a conventional silicon-based photovoltaic device [22]. This n-type layer limits contact resistance between the silicon and metal contact. Doping levels are controlled in order to maximize light collection and improve efficiency.

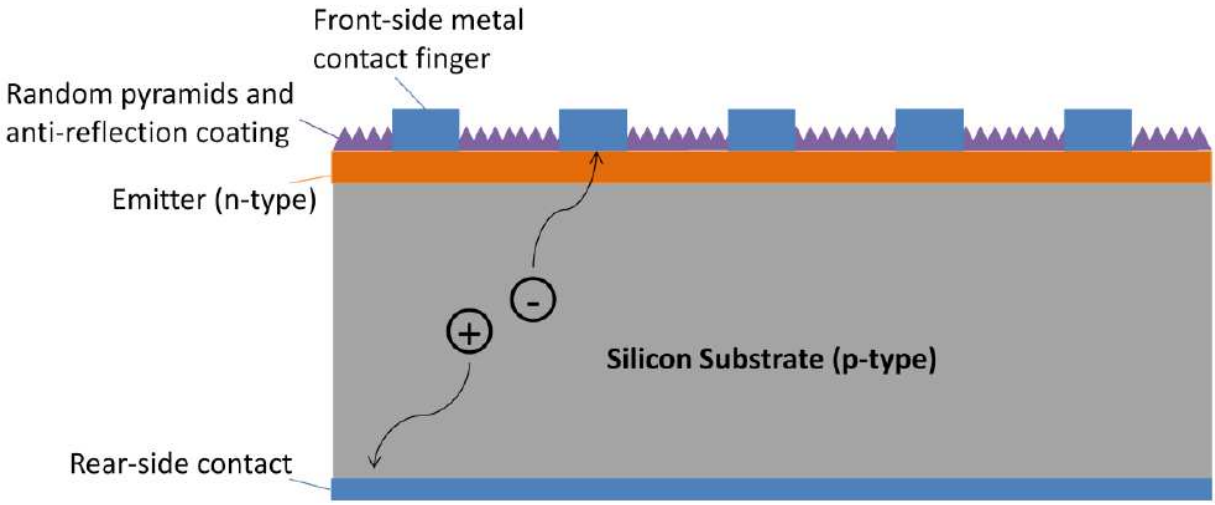

Figure 2. Schematic diagram of a conventional silicon-based photovoltaic device.

One of the limiting factors that reduce the use of photovoltaic cells is the cost of manufacturing relatively high efficiency cells. The primary interest in this thesis is the formation of selective emitters through the process known as laser doping. Selective emitters are structures that are formed on the front surface of silicon wafers, increase the performance of the device, and can lead to cost savings by requiring less metal for the contact grid. These structures have been known to increase efficiency, but only recently has a laser been used to perform one of the diffusion steps. Laser doping is a novel process, where a laser is used to heavily dope a localized region below the surface of the silicon. The use of a laser leads to faster processing times due to fast diffusion rates in the liquid phase.

Objectives

In order to understand the physical processes that occur during laser doping, a well-tested numerical heat transfer and fluid flow model is adapted to simulate the laser-silicon interaction during the formation of a selective emitter with a continuous wave, green (532 nm) laser beam. During laser doping, a molten pool develops, bulk fluid motion occurs, and mass transfer increases the dopant concentration throughout the pool. The molten pool geometry is important because these dimensions determine the depth and width of the selective emitter. Fluid motion and mass transfer influence the final distribution of dopant in the selective emitter, and this distribution will have a direct effect on the electrical properties of the wafer surface. The numerical model is validated with independent experimental data in terms of molten pool width

and depth, concentration profile, and sheet resistance. With a general understanding of the laser doping process, the variation of process parameters, travel speed and output power, on pool geometry dimensions, dopant distribution characteristics, and sheet resistance is examined with the aid of process maps. The major mechanism of mass transfer, either convection or diffusion, that drives the movement of dopant into the pool is examined through dimensional analysis.

Chapter 2: Literature Review

Selective Emitters and Photovoltaic Devices

A selective emitter is a 'structure' that is formed on the front surface of crystalline silicon wafers to enhance the efficiency of a photovoltaic cell. The high concentration of n-type atoms that characterizes a selective emitter decreases the contact resistance between the silicon surface and the metal contacts, which collect charge carriers during operation. A typical solar cell is made from a wafer with either a high concentration of n-type atoms, which decreases contact resistance, or a low concentration dopant on the front side, which enhances the collection of photons at lower wavelengths (~ 400 nm). Additionally, the metal contacts are formed by screen-printing with expensive silver pastes. With a selective emitter, the best of both extremes is realized because a high dopant concentration is confined to where only the metal contacts are formed, while a low concentration is present on the rest of the surface enabling better collection of visible light photons. These two regions of concentration and the position of the metal contact are shown in Figure 3. Since the selective emitter is highly conductive, self-aligning plating methods from solution can be used to form the metal contacts. This eliminates the need for silver pastes and can reduce costs in terms of materials.

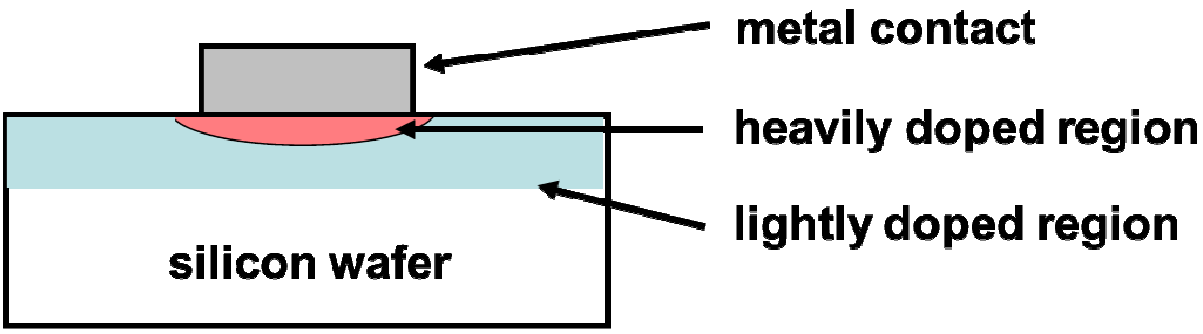

Figure 3: A schematic of the selective emitter structure contains the heavily and lightly doped regions and the metal contact.

Methods for Forming Selective Emitters

The four main methods for forming selective emitters include acid or plasma etching [23, 24], buried contact diffusion [25], diffusion masking [26], and laser doping [27]. Three of the methods are shown in Figure 4, where the white area is the silicon wafer, the blue area is the

lightly diffused region, and the red area is the heavily diffused region. Acid and plasma etching involves two diffusion steps. A light n-type diffusion step is followed by a heavy diffusion step. After diffusion, the front and back metal contacts are formed. Then, the heavily doped region between the contacts is etched away with an acid solution, hydrofluoric and nitric acids in the case of [23], or a plasma in a vacuum chamber.

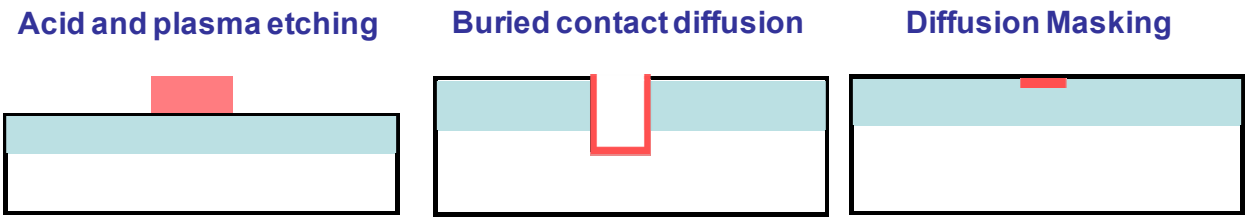

Figure 4: The final structures, without metal contacts, of the selective emitter during different formation methods are shown. The white area is the silicon wafer, the blue area is the lightly diffused region, and the red area is the heavily diffused region.

Buried contact diffusion requires forming grooves (20–30 μm wide and 50 – 100 μm deep) on the silicon wafer surface with either a mechanical grooving machine or a laser beam. Then, diffusion is carried out with a surface film dopant source. After a light etch to remove any remaining dopant film, top-surface metallization is performed, and the metal completely fills the grooves. In the case of diffusion masking, an oxide mask is formed on the silicon surface. This mask is then patterned into the grid shape using a pulsed laser to ablate the oxide. A heavy diffusion step forms the selective emitter in the now unmasked regions. The oxide mask is then removed through an etching step, and a second diffusion step forms a lightly doped layer on the rest of the surface. Laser doping is discussed in the next section and offers several advantages over the other three methods.

Laser Doping and the Laser-Silicon Interaction

The fourth method for forming selective emitters is laser doping, which is distinctly different from the other methods in one major way. The heavy diffusion step occurs in the liquid state. With a laser beam, the dopant source, anti-reflection coating, and silicon substrate are heated and dissociate or melt. While the molten silicon is present, the dopant atoms are incorporated into the molten pool through convection and fluid motion and liquid state diffusion, which has a diffusivity value that is four orders of magnitude greater than solid state diffusion.

The laser can be used in either pulsed or continuous wave (CW) mode. The surface of the silicon wafer is lightly doped in a diffusion step prior to laser doping. This method of forming selective emitters provides several advantages over the other methods, including the elimination of a high temperature diffusion step. Compared to the other methods, the selective emitter region can be much narrower, on the order of the beam diameter, < 20 μm, which after plating leaves more surface for light collection and, therefore, greater device efficiencies. Since the laser is the heat source, the entire wafer is not exposed to high temperatures during processing, and with the using of high speed scanning optics, the laser doping proceeds very rapidly. Laser doping offers several benefits and can reduce costs in terms of time, energy, materials, and device efficiency. Accordingly, several research groups have investigated laser doping as a way to form selective emitters.

Sugianto et al.[28] investigated the use of green lasers (λ = 532 nm) and near infra-red lasers (λ = 1064 nm) to selectively dope silicon. The group used a liquid spin-on-dopant as the dopant source and used the laser to fire through the dopant source and anti-reflection coating and into the silicon in order to achieve doping. The green laser with a travel speed of 0.5 m/s was found to perform best under the continuous wave conditions examined. An efficiency of 18.5 % was measured at an output power of 15 W and 0.5 m/s. The experimenters concluded that a green laser scanning over the silicon surface at speeds up to 6 m/s had been demonstrated as a fast processing method for forming quality selective emitters.

Tjahjono et al.[27] considered a Q-switched, 532 nm wavelength laser operating at 2 kHz for laser doping. A dried spin-on-dopant was used as the dopant source. The group also investigated the use of two different anti-reflection coating (ARC) materials, silica and silicon nitride. With the silica ARC layer, the group demonstrated an efficiency of 17.5 %, which was greater than the conventionally produced reference cell without a selective emitter. The silica ARC layer gave better performance than the silicon nitride layer.

Kohler et al.[29] used a novel rectangular laser beam with dimensions of 300 x 5 μm, in order to perform laser doping. The laser fired through a phosphosilicate glass layer (dopant source) to form the highly conductive part of the selective emitter. Compared to conventional cells, which were not laser doped and did not have a selective emitter, these laser doped samples exhibited a 0.5 % percent increase, absolute. Additionally, with a simple heat transfer numerical model, they showed the processing parameters required for certain peak temperatures and molten

pool depths. With these findings, it was concluded that this laser doping process can be implemented into an industrial setting (i.e. take less than 2 seconds to laser dope) as soon as pulsed green disk lasers achieve 600 W of output power.

Selective Emitter Characteristics and Laser Doping Parameters

There are several important selective emitter characteristics to consider when performing laser doping. Of these characteristics, the width and dopant depth have been shown to affect photovoltaic device performance. The width of the molten pool will define the width of the selective emitter, and this width will have an impact on the amount of front surface shading produced by the metal contacts. Consequently, smaller widths are desirable from a device efficiency perspective.

The depth of the molten pool will determine how far the dopant atoms diffuse into the silicon. From the literature, researchers have found that measurable amounts of dopant atoms at deeper depths lead to lower sheet resistances. Three authors [30, 28, 31] have investigated the relationship between the dopant depth and the sheet resistance. In all three cases, the sheet resistance was found to decrease with increasing dopant depth, which varied from 0.1 μm to greater than 3.5 μm. Sugianto et al. [28] used a CW 532 nm laser with speeds and powers ranging from 0.1 to 10 m/s and 9 to 15 W, respectively and found that the sheet resistance decreased by 86% when the depth increased from 2.4 μm to 3.5 μm. Schulz-Ruthenberg et al. [30] identified an 8% decrease in sheet resistance with an increase in depth of 0.30 μm from 0.43 μm with a 532 nm laser with various pulse lengths between 10 and 400 ns and powers ranging from 1 to 6 W. Paviet-Solomon et al. [31] performed laser doping with a 515 nm wavelength laser and a pulse duration of 20 ns and output powers ranging from 0.5 to 5.5 W. This research showed a 56% decrease in sheet resistance when the depth increased to 1.45 μm from 0.18 μm.

Other researchers [32, 33] have investigated the effect of dopant depth on the open circuit voltage (V_{OC}), short circuit current (I_{SC}), and the internal quantum efficiency (IQE) in the depth range of 0.2 to 0.5 μm. Both V_{OC} and I_{SC} are directly proportional to the solar cell efficiency, and the IQE is proportional to I_{SC}. Jager et al. [32] found that deeper dopant depths lead to higher open circuit voltages (V_{OC}) and therefore better performance. It was also found that deeper depths lead to lower IQE values at wavelengths below 800 nm [33]. The IQE is related to the short circuit current, so in this case deeper dopant depths lead to lower performance.

Researchers have shown that the dopant concentration profile can be controlled by the process parameters and that the profile has an effect on the performance of the silicon wafer in service.

Two other characteristics that can define a selective emitter are the average dopant concentration within the molten pool and the dopant concentration profile shape. The average concentration will be related to the volume of the molten pool and the time allowed for diffusion, while the dopant concentration profile will also be dependent on allowed time and the dimensions of the pool that will define dopant travel distances. These two parameters are easily modified and measured and should be considered in future work. Several groups have shown that the dopant concentration profile can be easily adjusted depending on the processing parameters such as pulse length and pulse energy or output power and travel speed [34, 35]. These profiles varied between nearly uniform profiles along the depth of the molten pool and typical graded profiles, where the concentration slowly decreases along the depth of the pool. Empirical relationships have been developed to calculate the sheet resistance if the dopant concentration profile is known [36, 37]. In this case, the sheet resistance is inversely proportional to depth, dopant concentration, and electron mobility.

Previous Laser Doping Modeling Efforts

Efforts have been made by researchers to model the dopant distribution profile produced through laser doping by numerically solving heat and mass diffusion equations [34, 38]. The main goal for numerically modeling the dopant concentration profile has been to show that numerical models can predict with reasonable accuracy the concentration profile. Kohler et al. used a two dimensional numerical model to solve for the temperature profiles and dopant distributions during laser doping with a 532 nm laser with a pulse length of 65 ns and a rectangular beam with dimensions of 200 x 5 μm, Figure 5. Good agreement between experimental and numerical results was found under various processing conditions such as pulse energy, pulse separation length, and number of scans.

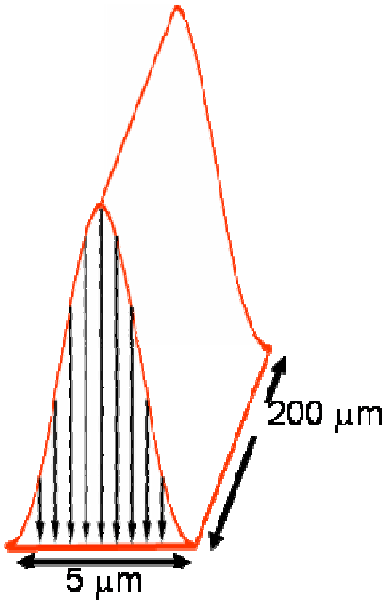

Figure 5: Kohler et al. [34] used a rectangular beam to laser dope silicon.

Poulain et al. used the commercial COMSOL® software, which is designed to simulate a variety of physical processes, to solve heat and mass transport equations to determine the temperature and dopant distribution profiles that result from laser doping of silicon with a 355 nm laser beam and a 10 ns pulse length. Good agreement between the calculated and experimental values was found at higher pulse energies (5 J/cm^2). In both cases, researchers were able to successfully simulate heat transfer and dopant incorporation during laser doping. Although both sets of researchers were able to develop and validate a model, fluid flow arising from the Marangoni effect and the temperature coefficient of surface tension was not considered. Fluid flow is expected to enhance mixing of the dopant and molten silicon to a certain extent depending on the fluid velocity and time available for mixing. In addition, the research only investigated the use of a pulsed laser beam to determine the dopant profile and did not discuss the size and shape of the molten pool. The work behind this thesis uses a three-dimensional numerical heat transfer and fluid flow model that solves for temperature and velocity fields to investigate the size and shape of the molten region and the evolution of the dopant distribution during the formation of the selective emitter by laser doping.

Chapter 3: Experiments and Model Development

High Power Laser Diagnostics

A Primes® Beam Monitor and a Primes® Focus Monitor[1] were used to characterize high power laser beams produced by an IPG Photonics[2]® YLR-12000 solid state ytterbium fiber laser, which operates at a wavelength between 1070 nm and 1080 nm and has a maximum output power of 12 kW. The beam was delivered to different sets of transmissive and reflective optic systems through an Optoskand®[3] 300 μm diameter process fiber with a divergence angle <200 mrad at powers ranging from 500 W to 12 kW. All of the optical setups were monitored for times up to ten minutes. Over this period of operation, the beams were characterized at selected time intervals, and changes in the beam properties were monitored.

A Precitec® YW50 welding head was used in this study as the transmissive optic system and is composed of a collimator and a focusing lens. Collimators are primarily defined by the distance between the process fiber and the entrance to the collimator. The magnitude of this distance is designed to ensure that the beam divergence from the process fiber is sufficient to produce a beam that is the correct size for the collimating lens. A 200 mm focal length Precitec[4]® collimator (COL YW50 200 QBH ZK) was used. The collimator was characterized at three different powers (4, 8, and 12 kW) and distances ranging from 100 mm to 500 mm from the collimator exit plane using the Primes® Beam Monitor to determine the degree of collimation of the beam. Precitec® 200 mm and a Precitec® 500 mm focal length fused silica focusing lenses were also analyzed in this study. The beam was monitored at locations both above and below the focal point in order to measure the beam propagation parameters. The 200 mm focus length system was not characterized at an output power higher than 8 kW in order to not exceed the limit on the allowable peak power density (10 MW/cm^2) of the Primes® Focus Monitor.

A reflective optics system produced by Laser Mech®[5] was also analyzed as part of this study. This system consisted of a 125 mm focus length collimator (part # PLFXT0020) and a 600 mm focus length focusing mirror (part # PLFPCXXXX). The optical mirrors in this system

[1] Primes GmbH, Pfungstadt, Germany
[2] IPG Photonics Corporation, Oxford, MA
[3] Optoskand AB, Molndal, Sweden.
[4] Precitec Group, Gaggenau, Germany
[5] Laser Mechanisms, Novi, Michigan.

are made from polished copper and use parabolic surfaces to direct, collimate, and focus the laser light. This system was characterized in the same manner as the transmissive optics, with the collimated beam being characterized at different distances from the collimator exit and the beam exiting the focus optic being characterized at several locations above and below the sharp focus setting.

In two of these optics systems, a different focal length collimator and focus optic combination is used. The combination of different focal length collimator and focus lens in the optical system leads to the introduction of an optical magnification factor [29] that affects the magnitude of any change in focus length of the system. Abt et al [7] showed that the change in focal length of the laser system (Δf_{laser}) is proportional to the square of the quotient of the focus length of the focusing optic (f_{foc}) and the focus length of the collimating optic (f_{col}), as shown in Equation (1):

$$\Delta f_{laser} \sim \left(\frac{f_{foc}}{f_{col}} \right)^2 \sim \beta^2 \tag{1}$$

where β is the optical magnification. The impact of the optical magnification factor becomes more prominent when dealing with long focal length optics, in which the collimator typically has a much smaller focal length than the focusing optics. In these systems, the larger optical magnification factor can cause larger shifts in the focal length compared to an optical system with a magnification factor of one.

The optics systems of interest in this study were characterized using a pair of beam diagnostic tools. The Primes® Beam Monitor characterized the beam exiting the process fiber and collimator, and the Primes® Focus Monitor was used to characterize the beam near the focal point. These Primes® systems, which can be classified as rotating pinhole diagnostic devices, provide relatively fast data collection and comprehensive characterization results. In the case of the Primes® Beam Monitor, the beam enters the device through a 100 mm diameter opening and strikes a small mirror attached to the end of a hollow spinning aluminum rod, which then directs a small amount of laser light to the photodiode detector. This device measures the beam diameter at a single distance from the fiber or collimator exit and is best suited for measuring beam diameters between 12 mm and 90 mm [40].

The Primes® Focus Monitor operates on the same principle as the Beam Monitor but uses a pinhole, with a diameter of approximately 30 μm, instead of a small mirror, allowing it to measure beam diameters between 0.1 mm and 6 mm. This tool takes measurements along multiple planes in the beam path to determine the focus position. Using the data obtained during these measurements, the focus distance, beam width at focus, divergence angle, and Rayleigh length are calculated. Because of the small size of the pinhole and the coatings used in the probe tip, the peak power density of the beam which can be measured with this device is limited to 10 MW/cm^2.

During the collection of the beam data by the Primes® diagnostic instruments, nearly all of the beam energy passes through the diagnostic measurement area and not to the instrument detector. At high powers, a great deal of heat can be generated by directing the laser into a graphite block (150 mm diameter and 60 mm thick). In order to ensure that the heat radiated from the graphite block is sufficiently dissipated and does not introduce potential error into the measurements, it was submerged in circulating water, as shown schematically in Figure 6. In the experimental set up, cold water flows continuously into the tub using 15.9 mm diameter hoses and circulated using a Pacific Hydrostar® pump at a maximum rate of 125 L/min to maintain a nearly constant water level. In addition, the characterization measurements were spaced to ensure that any heat accumulated during a measurement was dissipated before the next. For characterization of the initial propagation parameters, the laser was operated for up to 15 s in order to perform a measurement and then allowed to cool for 60 s. For consecutive measurements where the laser was operated continuously up to 10 minutes, the system cooled for 5 to 20 minutes depending on the operation time.

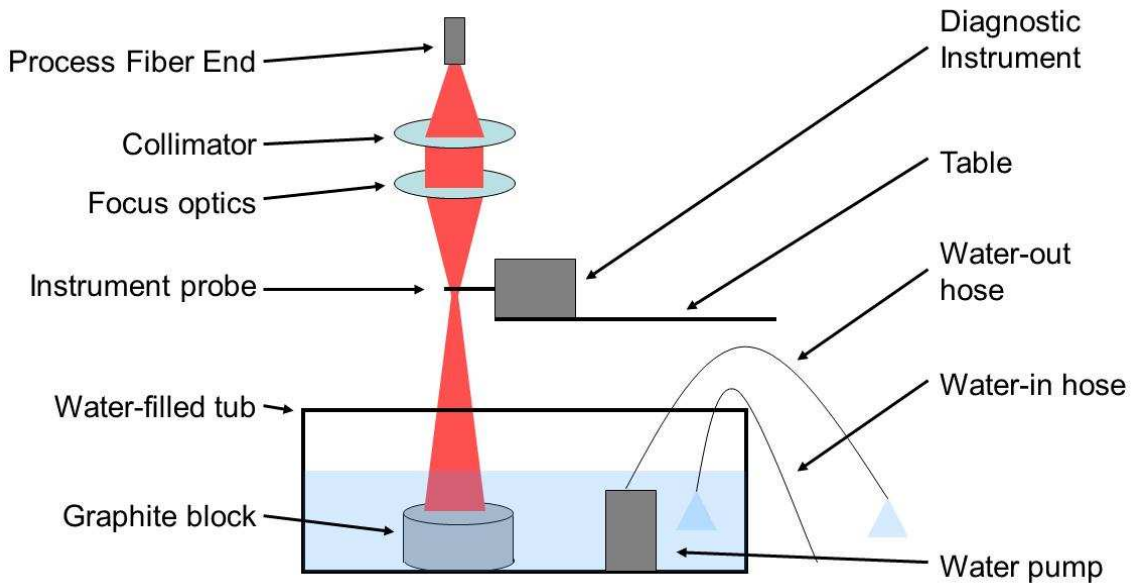

Figure 6: Schematic diagram showing the experimental setup used to obtain beam diagnostic data and mitigate any error associated with excess heat caused by the interaction of the beam with the graphite block.

After the data are obtained by each diagnostic tool, the Primes® Laser Diagnose Software computes the beam width and other beam parameters. All beam measurements are made in a square measurement window comprised of a user defined number of pixels where the intensity counts are recorded. The measurement resolution of this device is a function of the measurement window size and the number of pixels within the window and is expressed in terms of length per pixel (mm/pixel). Only changes in beam diameter greater than the 30 µm diameter pinhole or the measurement resolution (whichever is greater) can be considered to be significant. Any changes below this value are a result of small calculation differences resulting from minute changes in the recorded power density distributions between any two measurements. Typical resolution values range from 16 µm to 125 µm for the Focus Monitor and 100 µm to 500 µm for the Beam Monitor.

Collection of the power density distribution in one plane along the beam propagation direction allows several parameters (beam diameter, peak power density, kurtosis) to be calculated using statistical methods. If several beam distributions are collected at selected planes along the propagation direction, the beam can be reconstructed mathematically and beam propagation parameters, such as the focus length, diameter at focus, divergence angle, and Rayleigh length (i.e. the distance from focus where the beam area doubles) can be calculated.

The width of the laser beam is the primary beam characterization parameter. There are numerous ways to determine the beam width [13, 41, 42]. Usually, the beam diameter is a measure of how much energy is contained within a one dimensional beam profile of the power density distribution, as shown in Figure 7. Two common definitions involve the $1/e^2$ and the full width at half the maximum (FWHM), both of which define how fast the energy density decreases from the peak energy density. In both definitions, the energy distribution is assumed to be either a standard Gaussian or top hat distribution. However, the beam does not always take these specific forms but is some combination of the two and may contain other asperities, e.g. astigmatism, making it difficult to easily define a universal beam diameter.

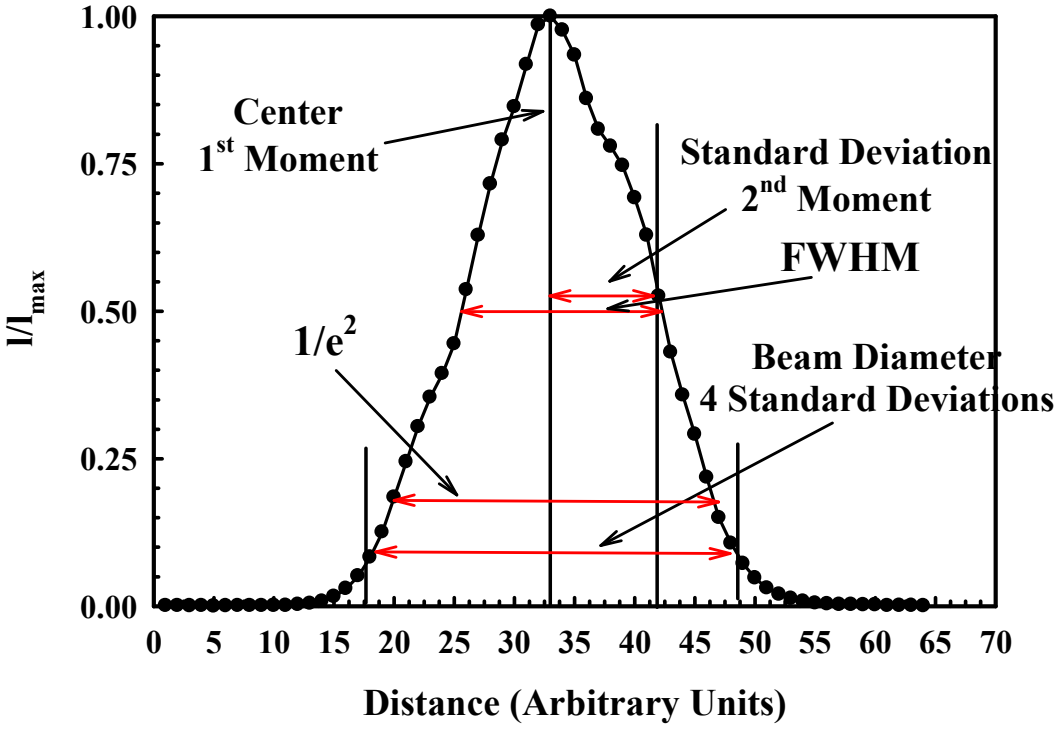

Figure 7: A one dimensional laser beam power density distribution with the ISO definition of beam width is shown.

A more comprehensive beam width definition has been codified in ISO 11146 [42]. In the ISO procedure for determining the beam diameter, the beam center or 1st moment is defined as the mean of the distribution, and the 2nd moment is similar to the variance of a probability

distribution. From the variance, the standard deviation is determined, and the beam diameter is defined as being four times the standard deviation as shown in Figure 7. The 2nd moment, or variance, definition is the output from the Primes® diagnostic tools.

Experimental Data from Literature

The experimental procedure, system, and data that are used to validate the model were published by Sugianto et al.[28] The system consisted of a 180um thick n-type silicon wafer coated with a 75 nm SiN_x passivation and anti-reflection (AR) layer, and 45 mass% phosphoric acid solution spin-on-dopant with an approximate thickness of 0.5 μm. A schematic of the layout of the silicon wafer and layers is shown in Figure 8.

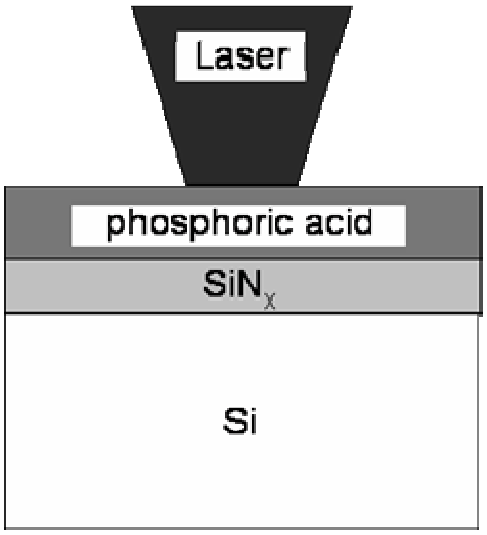

Figure 8: The material system consisted of a silicon substrate, an AR coating of SiN_x, and a doping layer of phosphoric acid.

To perform the laser doping, a Spectra-Physics Millennia Prime® laser operating at a wavelength of 532 nm with a maximum output power of 15 W in a continuous wave mode was used. The reported beam diameter was 20 μm with a Gaussian intensity distribution at the surface of the sample.

Heat Transfer and Fluid Flow Model

For mathematical modeling, a well tested finite difference based model is employed [43-49] to solve for the temperature and velocity fields in the molten pool. A typical calculation domain was 1000 μm x 250 μm x 250 μm with irregular sized rectangular control volumes of 245 x 95 x

55. Minimum grid spacings of 0.2 μm were used in the molten region to achieve a maximum resolution of variables. The equations of the conservation of mass, momentum, and energy are solved in the model. Figure 9 shows the computational domain with the six surfaces identified and three axes labeled.

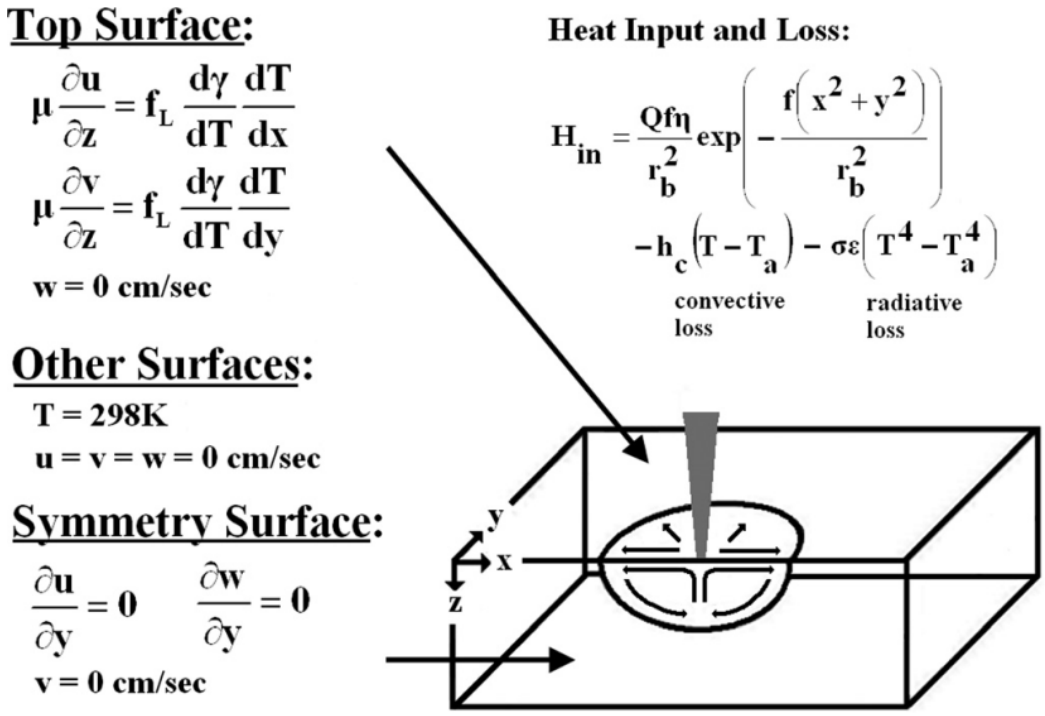

Figure 9: The computational domain consists of the south symmetry plane and the top plane where the heat source is implemented.

The conservation of mass, or continuity, equation is shown below:

$$\frac{\partial(\rho u_i)}{\partial x_i} = 0 \qquad (2)$$

where ρ is the density of the liquid, u_i is the velocity in the i^{th} orthogonal direction (i = 1, 2, or 3), and x_i is the distance along the i^{th} axis. The conservation of momentum is solved using the Navier-Stokes equation, which is expressed as:

$$\rho\frac{\partial(\rho u_j)}{\partial t} + \frac{\partial(u_j u_i)}{\partial x_i} = \frac{\partial}{\partial x_i}\left(\mu\frac{\partial u_j}{\partial x_i}\right) + S_j \qquad (3)$$

where u_j is the velocity component in the j^{th} direction, t is time, μ is the viscosity, and S_j is the source term for the j^{th} direction.

The conservation of energy is:

$$\rho\frac{\partial h}{\partial t}+\frac{\partial(u_i h)}{\partial x_i}=\frac{\partial}{\partial x_i}\left(\frac{k}{C_p}\frac{\partial h}{\partial x_i}\right)-\rho\frac{\partial(\Delta H)}{\partial t}-\rho\frac{\partial(u_i\Delta H)}{\partial x_i} \quad (4)$$

where h is the sensible heat, k is the thermal conductivity, C_p is the specific heat, and ΔH is the latent heat of fusion. These equations are discretized, and then the dependent variables, enthalpy, velocity, and dopant concentration are calculated using the tri-diagonal-matrix algorithm (TDMA) [50].

The energy distribution of the beam at positions x and y is defined using the following relationship [51]:

$$H_{in}=\frac{qf\eta}{\pi r_b^2}\exp\left(-\frac{f\left(x^2+y^2\right)}{r_b^2}\right) \quad (5)$$

where q is the total beam power, η is the absorption of the material at the given wavelength, r_b is the radius of the beam at the sample surface, and f is the distribution factor, which determines the peak intensity of the beam. Since the beam has a Gaussian distribution, the value of f is set to two for these simulations. Due to the relatively low concentration of phosphorus in silicon in this work, less than 0.05 wt.%, the binary Si-P system has not been considered here. These low concentrations will not impact the liquidus and solidus temperatures like the conditions considered in similar recent research [52]. Table 1 lists the properties and values used in the calculations.

Table 1: The properties and values used in the calculations are listed.

Property	Value	Reference
Density of liquid Si (kg m^{-3})	2570	53
Absorbtivity of liquid Si	0.234	54[a]
Effective viscosity (kg m^{-1} s^{-1})	0.0074	55,56,57
Melting temperature (K)	1687	58
Enthalpy of solid at melting point (kJ kg^{-1})	1280	59
Enthalpy of liquid at melting point (kJ kg^{-1})	3079	59
Specific heat of solid (J kg^{-1} K^{-1})	891	59
Specific heat of liquid (J kg^{-1} K^{-1})	1004	59
Thermal conductivity of solid (J m^{-1} s^{-1} K^{-1})	36	60
Effective thermal conductivity of liquid (J m^{-1} s^{-1} K^{-1})	56	60,61,62
Coefficient of thermal expansion (K^{-1})	2.60E-06	62
Temperature coefficient of surface tension (mN m^{-1} K^{-1})	-0.13	55
Enthalpy to heat and vaporize acid dopant layer (kJ kg^{-1})	5068	59
Enthalpy to heat and disassociate SiNx AR layer (kJ kg^{-1})	972	59,63

[a]Values were extrapolated from [54].

AR and Dopant Layers and Model Development

The energy to heat and dissociate SiN_x and heat and vaporize the acid solution is accounted for by calculating the area and length of the molten pool. The area of the pool and the thickness and density of the layers are used to calculate the energy needed to heat and vaporize or dissociate the layers. In order to determine the amount of energy deposited over the length of the pool, laser power, pool length, and scan speed are considered. The ratio of the energy needed for heating and transforming the layers to the energy deposited over the length of the pool is subtracted from the energy absorbed by the silicon, as shown below:

$$H_{in}^{'} = H_{in}(1 - ratio) \tag{6}$$

The ratio is defined below:

$$ratio = \frac{A(\rho_{SiN_x} h_{SiN_x} E_{SiN_x} + \rho_{acid} h_{acid} E_{acid})}{q\eta L / v_{beam}} \tag{7}$$

where A is the area of the molten pool, ρ is the density of the layers, h is the thickness of the layer, E is the energy per unit mass to heat and transform the layers, L is the length of the molten pool, and v is the beam scan velocity. A schematic of the pool area and length is shown in

Figure 10, which illustrates the energy needed to vaporize and dissociate the layers, proportional to the area, and the energy deposited by the beam, proportional to the length of the pool and the velocity of the beam. With thicker layers or a larger molten pool area, more energy will be required to heat and melt the layers. Also shown in Figure 10 is the area/time ratio vs. travel speed at several powers. The surface area of the molten pool is proportional to the amount of energy required to heat and vaporize the layers, and time (length of the pool/beam travel speed) is proportional to the amount of energy deposited over the length of the pool. The ratio increases with travel speed because there is less time and, therefore, less energy at any given power level. At higher powers, the area of the molten pool increases, so the ratio also increases.

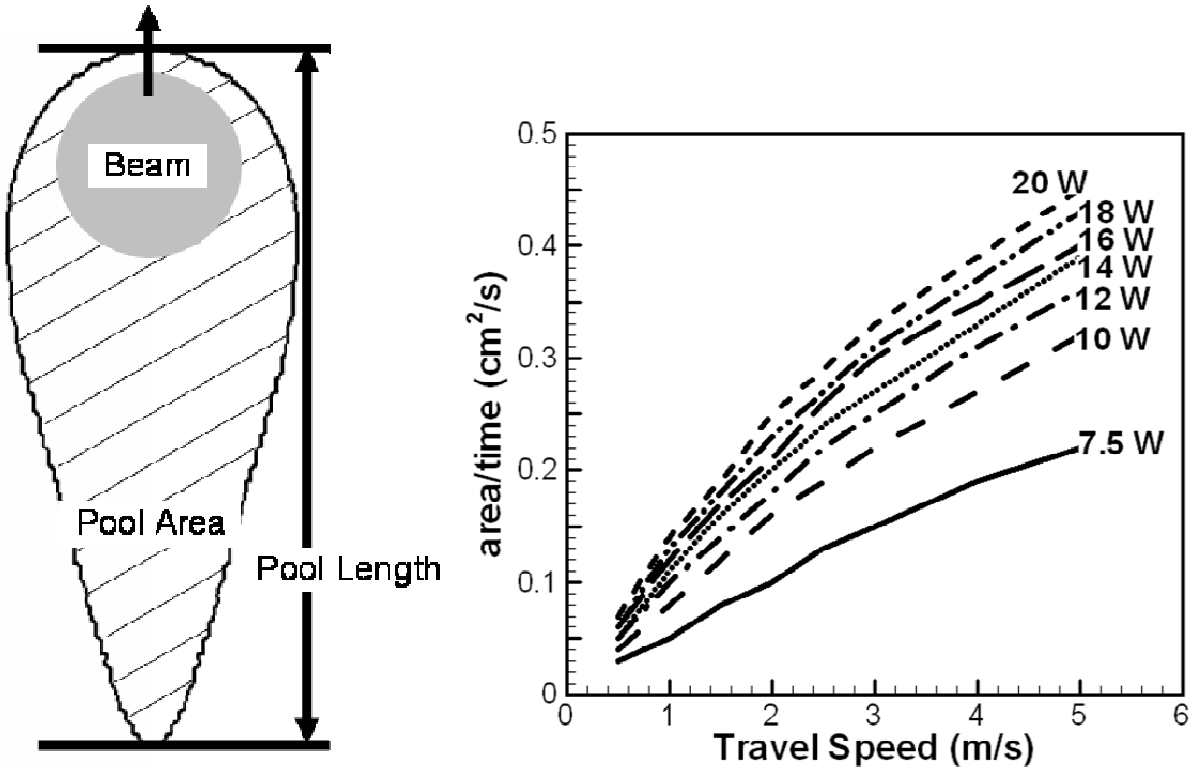

Figure 10: This schematic shows how the energy needed to heat and melt the layers was subtracted from the total input energy.

When considering another material besides the base material, phosphorus in this case, many times a binary alloy must also be considered. One of the main differences between a pure material and an alloy is the presence of liquidus and solidus temperatures in the alloy. These temperatures are determined by the binary alloy phase diagram shown in Figure 11 [64]. The

highest concentration of phosphorus is less than 0.06 wt%. This puts the alloy within the solid solubility of silicon, and such a low concentration will not lead to significantly different solidus and liquidus temperatures. In this case, the melting temperature of silicon 1687 K is the solidus and liquidus temperatures. If the concentration of the second component is greater or there is a lack of solid solubility, then a binary alloy must be considered [52].

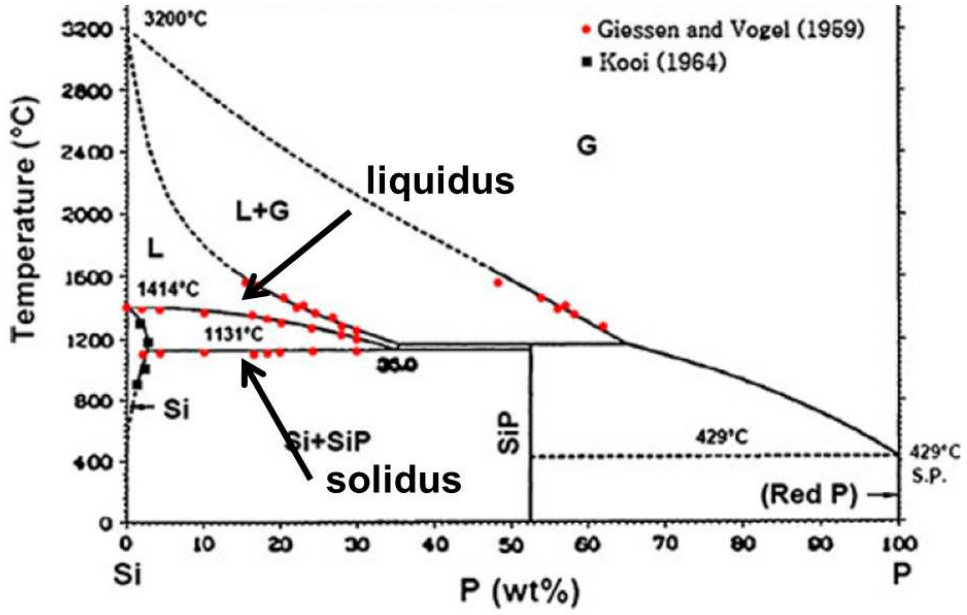

Figure 11: The Si-P binary phase diagram is shown. With very low concentrations of phosphorus, the solidus and liquidus temperatures are assumed to be equal because of the solid solubility of phosphorus in silicon.

Model Validation on Pure Silicon

The model was validated with pure silicon using an IPG near IR (λ = 1070 nm), fiber laser. The power ranged from 20 W to 40 W, and the scan speed and beam diameter were kept constant at 25 mm/s and 130 μm, respectively. Figure 12 shows the top surface of the silicon after laser processing.

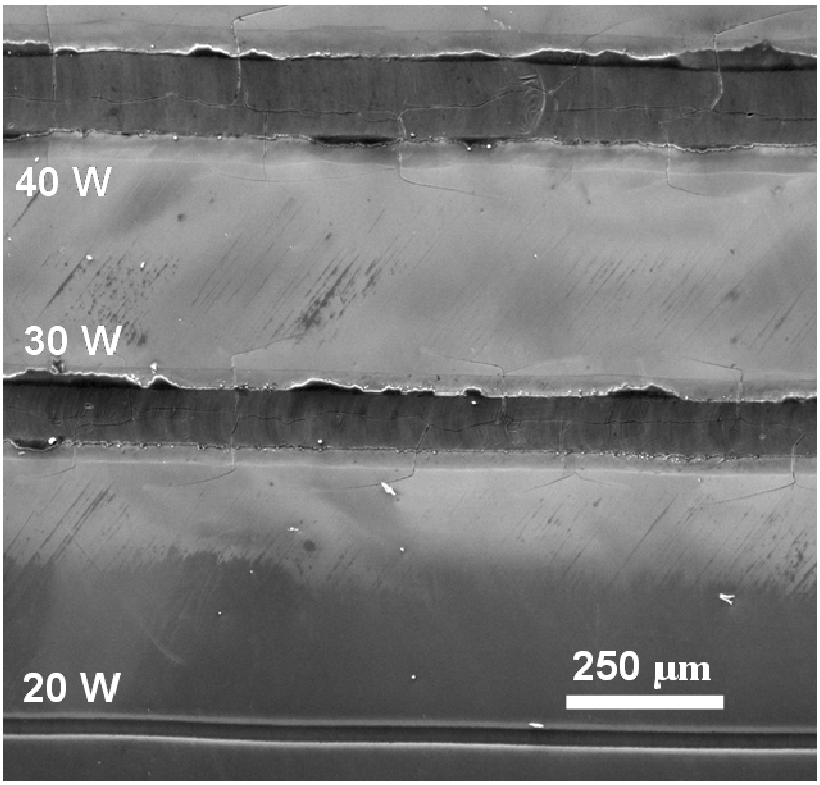

Figure 12: Micrograph shows experimental laser scans on silicon at various powers with a 130 µm beam at a travel speed 25 mm/s.

The molten pool widths at 20, 30, and 40 W were 26, 88, and 129 µm, respectively. At the two higher powers, a substantial number of cracks were apparent within and just outside of the molten region. In order to validate the model with pure silicon, the experimental and calculated molten pool widths are compared in Figure 13. Good agreement is obtained at the two higher powers, but at 20 W, the widths are much different. With general agreement between the numerical model and physical experiments, the model can be modified and then validated with faster scan rates with a frequency doubled laser.

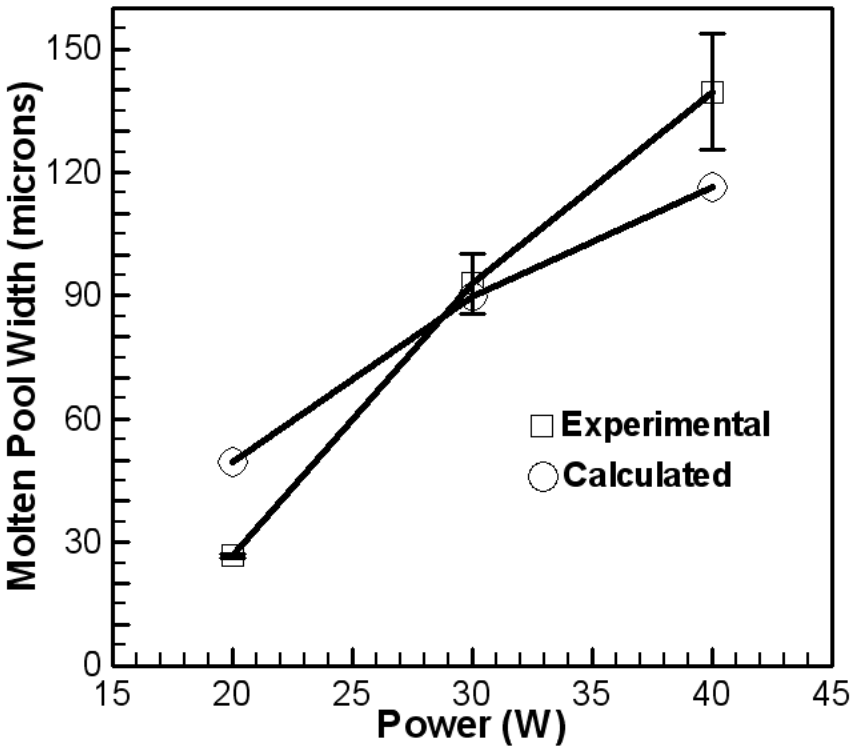

Figure 13: The experimental and calculated molten pool widths show moderate agreement, especially at the higher two powers.

Chapter 4: Results and Discussion

High Powered Laser Diagnostics

Characterization of Process Fiber

The process fiber transports the beam from the laser to the collimating and focusing optics. Properties of the fiber are specified in the diameter of the fiber core and the divergence of the beam out of the fiber exit. With the Primes® beam monitor, the diameter of the beam was measured at several distances from the end of the process fiber. The results are shown in Figure 14. The blue line shows how the beam diameter will change for a beam divergence of 200 mrad, which corresponds to the upper limit of the manufacturer specified divergence. The measured beam diameters increase as a linear function of distance. Initially changes in power, however, do not have a measurable effect on the beam diameter or divergence.

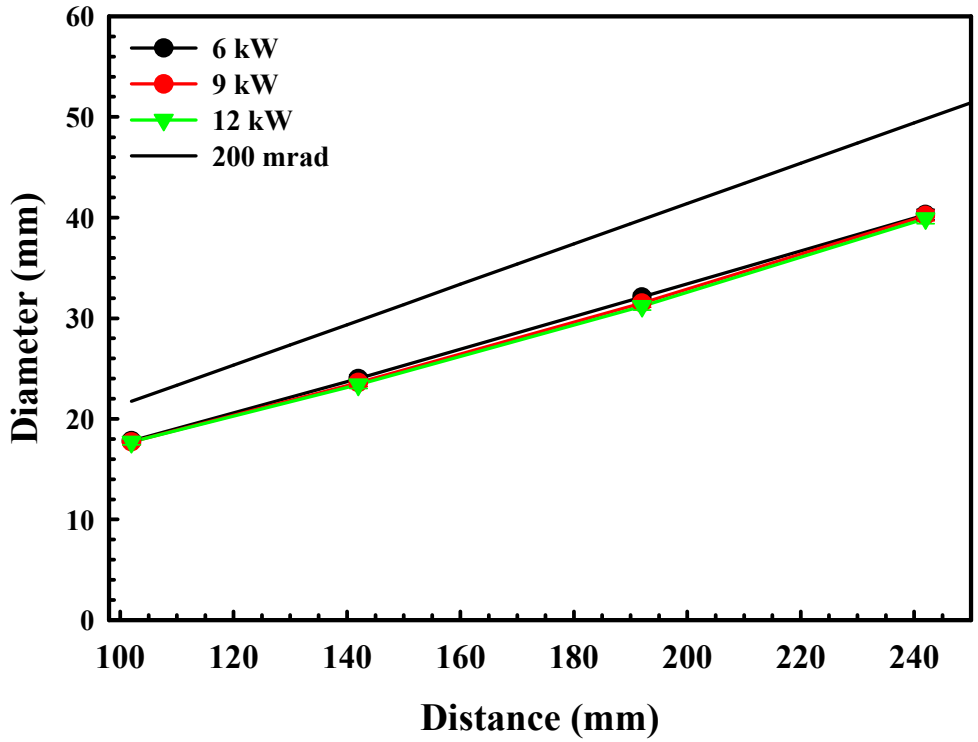

Figure 14: Graph showing the beam diameter measured at several distances from the exit of the 300 µm fiber (fiber end plane) for three different laser power levels immediately after the laser is turned on. The blue line represents the calculated beam diameter for a fiber divergence of a manufacturer specified 200 mrad.

The slope of a line fitted to the beam diameter measurements at four distances, gives the half angle of divergence. Based on these measurements, the angle of divergence at time zero is 160 mrad, which is much lower than the manufacturer specified value of < 200 mrad. This difference in divergence angle has a measurable impact on the size of the beam entering the collimator. For example, at a distance of 200 mm from the fiber exit, the beam is measured to have a diameter of 32 mm, as compared to a beam diameter of 40 mm if a value of 200 mrad is used. As a result, the beam is much smaller than expected, and only 44% of the lens clear aperture is filled, as compared to 69% with the 200 mrad beam divergence. At high laser powers, this smaller and more concentrated beam can lead to localized heating of the collimating and focusing optics producing a different beam size than expected.

Figure 15 shows how the full angle divergence changes as a function of time at three powers with the error bars representing the maximum error from the measurement resolution that could be carried through in the divergence angle calculation. At each power, the angle decreases with time, and as the power increases, the decrease in the divergence angle becomes larger.

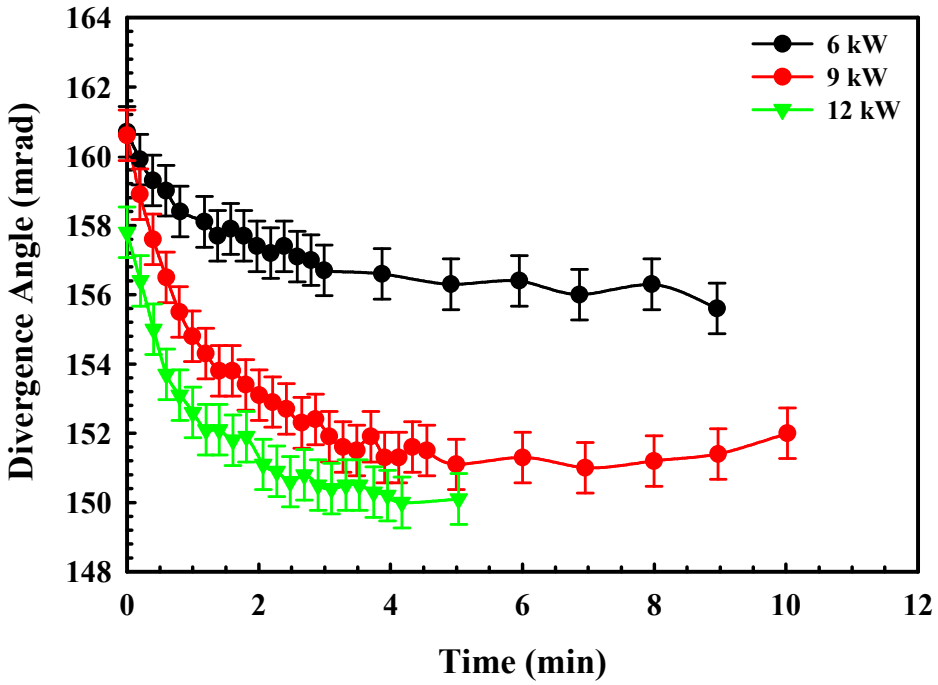

Figure 15: Graph showing changes in the divergence angle of the beam exiting the 300 µm process fiber as a function of time at three different powers.

These changes in divergence angle at these high powers result in a change in the beam diameter entering the collimator. For example, at 6, 9, and 12 kW, the angle decreases 5, 9, and 8 mrad, respectively, with continuous operation. At 9 kW and 12 kW, this change in divergence angle can result in a beam diameter change of approximately 2 mm at 200 mm from the end of the fiber, where the beam enters the collimator. Since the lens size is optimized for the diameter of the beam incident on its surface, the focusing potential of the lens is decreased, and the lens may heat more than it should because the laser energy is confined to a smaller area.

Characterization of the Focus Optics

The focus optics direct the collimated laser light to a very small region (less than 1 mm in diameter) on the workpiece over a certain focus length, so focus optics are typically characterized by the diameter of the beam at the focus position and the focus length. An important concern is the stability of the optics with time since lasers in a manufacturing setting can by on for more than an hour. The 200 mm focus length optics showed very little change with time. However, welding and deposition processes are frequently performed using defocused beams, and changes in beam properties under these conditions can result in undesired changes in weld or deposition properties. The impact of prolonged exposures to high laser power at locations 6.35 mm above and below the focus position, which is about 2.5 times the Rayleigh length, have been examined. Figure 16 shows the changing beam diameter with time at 8 kW and the beam profiles obtained at the beginning and end of the three minute run.

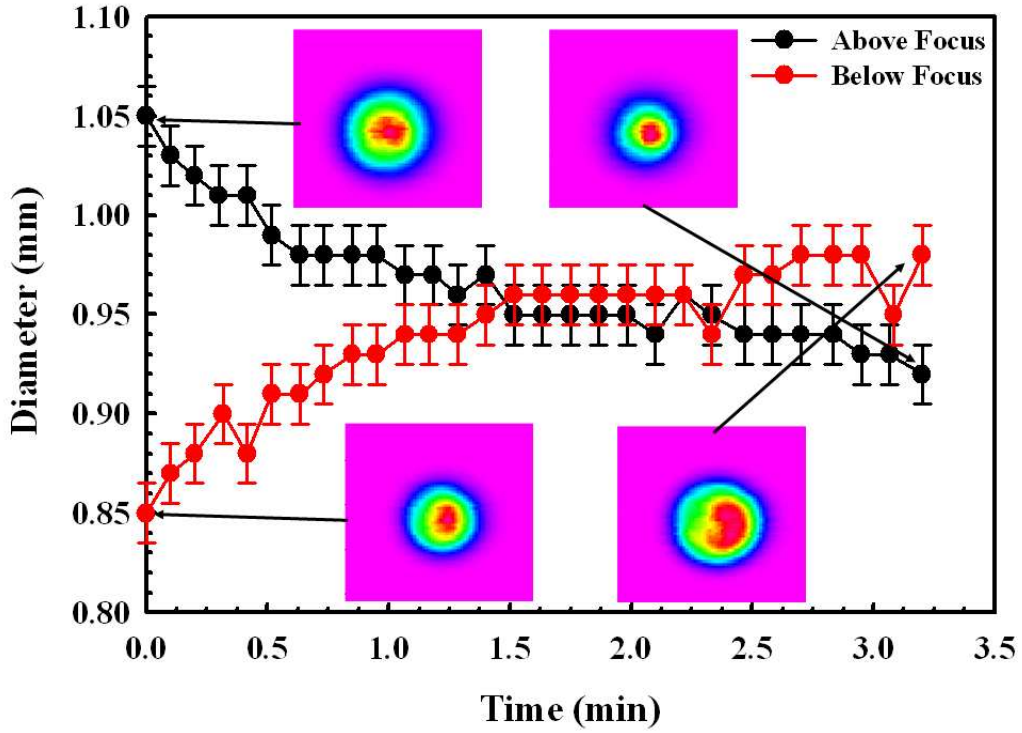

Figure 16: Graph showing changes in the beam diameter with time at 6.35 mm above and below focus with the 200 mm focal length optics at a power of 12 kW. The initial and final beam profiles at each position are also shown.

At these times, the changes in beam diameter are -0.124 and +0.130 mm for positions above and below focus, respectively. These changes in beam diameter are much larger than the measurement resolution (0.030 mm) and correspond to a 1 mm decrease in effective focus length. The beam diameter measured above focus decreases because the focus position of the system is moving closer to the measurement plane, and the beam is moving 'into focus' at that position. Conversely, at positions below focus, the beam is moving further out of focus, and the beam diameter increases.

The beam exiting the 500 mm focus length optic was also monitored at focus over three minutes of continuous operation at various power levels, and the results are shown in Figure 17. All measurements in this figure have a 30 μm resolution. At powers of 4.5 and 9 kW, the beam diameter showed a minimal change over the three minutes of monitoring, but at 12 kW, the diameter increases 0.158 mm, which is a 20% increase over the initial diameter. This increase corresponds to a nearly 8 mm decrease in effective focal length, which is 60% of one Rayleigh length.

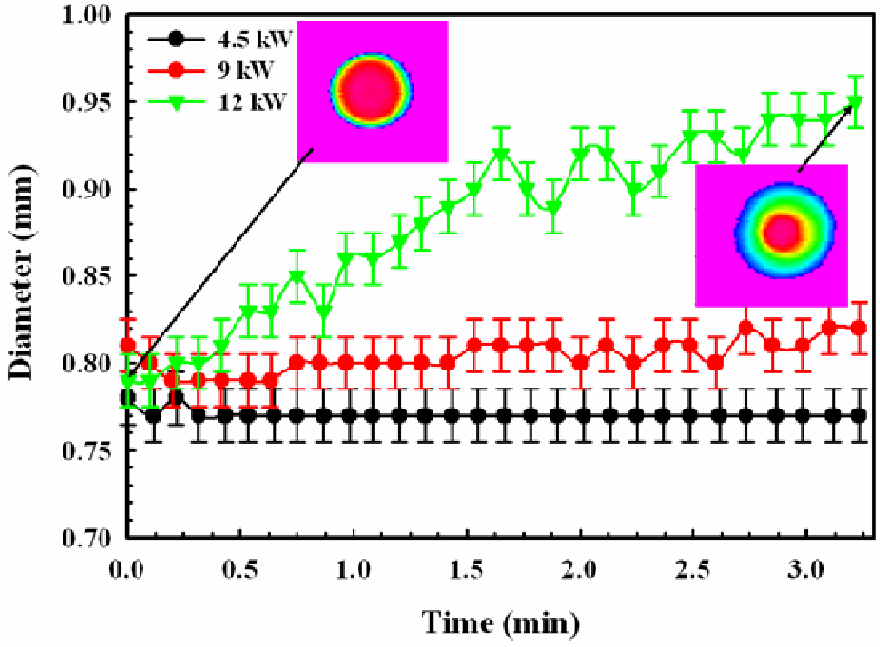

Figure 17: Graph showing changes in beam diameter at focus at different power levels with the 500 mm focus optic configuration. The beam profiles obtained at times of 0 minutes and 3 minutes at 12 kW of output power are also shown.

The two dimensional beam profiles at 0 minutes and 3 minutes for the 12 kW power level show that the general shape of the beam also changed from a top hat to a Gaussian beam profile. A Gaussian beam will have a higher peak power density than a top hat beam of the same diameter and power. A changing beam profile means a changing intensity distribution, which can have a major impact on process results if the process is sensitive to the beam power density distribution. This profile change is the reason the peak power density, which depends on the diameter and shape of the beam, did not decrease more than 5%, while the average power density decreased 30%. The beam profile changes because the beam is moving out of focus at the measuring plane. Under normal conditions, the optics produce a top hat beam at focus, but at locations outside of focus, the beam takes a more Gaussian type distribution.

Impact of Damage to Transmissive Optics

Under normal operating conditions, the laser optics can become damaged, and due to the nature of commercial optics (i.e. assembled in an enclosed head), this damage may not be immediately obvious to the laser operator. Any damage to the optics can have detrimental impact on the quality of the laser processed workpiece. A collimator was damaged in service at the Applied Research Lab. Some of the anti-reflection coating was removed, leaving a non-uniform covering on the lens. The propagation parameters were characterized with the damaged collimator and normal focus optics. Instantaneous parameters were unchanged, so the focus length, beam diameter at focus, and Rayleigh were the same as the undamaged case at time zero.

Changes in the beam diameter at initial focus were monitored as the laser was allowed to run continuously for up to seven minutes. The 200 mm focal length optics were operated continuously for six minutes at 0.5, 4, 5, and 6 kW. Figure 18 shows the diameter changes over six minutes using these optics. At 500 W, there was no measurable change in beam diameter. As the power level increases to 4 and 5 kW, changes in the beam diameter begin to appear, and by 6 kW, the beam diameter more than doubled in size after six minutes of laser operation. In addition to the dramatic increase in beam diameter, the beam profile changed as well, as shown in Figure 18. The area of maximum intensity in the beam profile at 6 kW became oblong during continuous operation, and the lower part of the profile lost a significant amount of power. These changes in the beam profile will have an undesired impact on the quality of the resulting weld or clad that may or may not be detectable during processing.

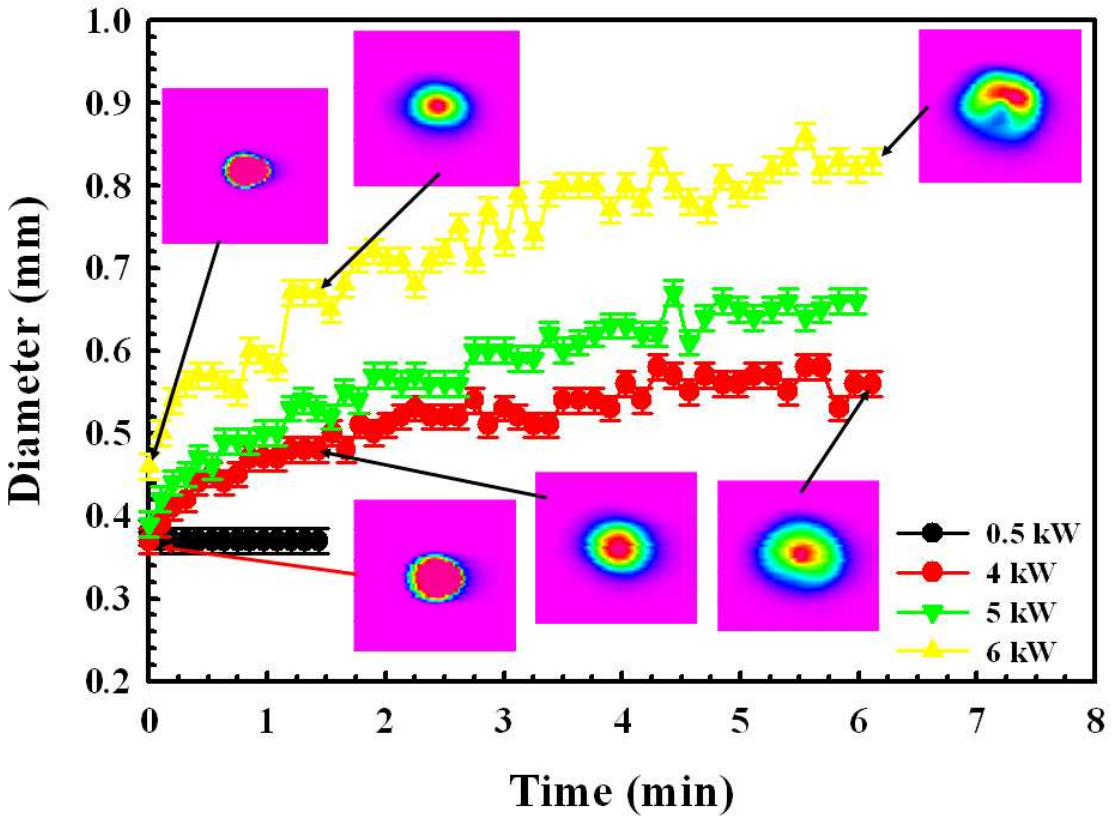

Figure 18: Graph showing the measured changes in the focused beam diameter as a function of time at selected powers for the 200 mm focus optics using a damaged collimator. The measured beam profiles at selected times at powers of 4 kW and 6 kW are also shown.

The 500 mm focal length optics with the damaged collimator was also characterized at powers of 6, 9, and 11 kW during continuous operation of four to seven minutes. Figure 19 shows the diameter changes during continuous operation of the laser. As expected, the diameter change is greater at higher power, with the beam diameter doubling in size after 7.5 minutes at 6 kW and quadrupling in size after four minutes at 11 kW. There was also a beam profile change as shown in Figure 19. The beam at 11 kW starts out in a nearly top hat profile and in less than one minute is no longer circular, and the beam shape cannot be described as either strictly Gaussian or top hat. After four minutes, the beam has a 'hole' in the center of its profile where very little energy is located and three areas of high peak intensity.

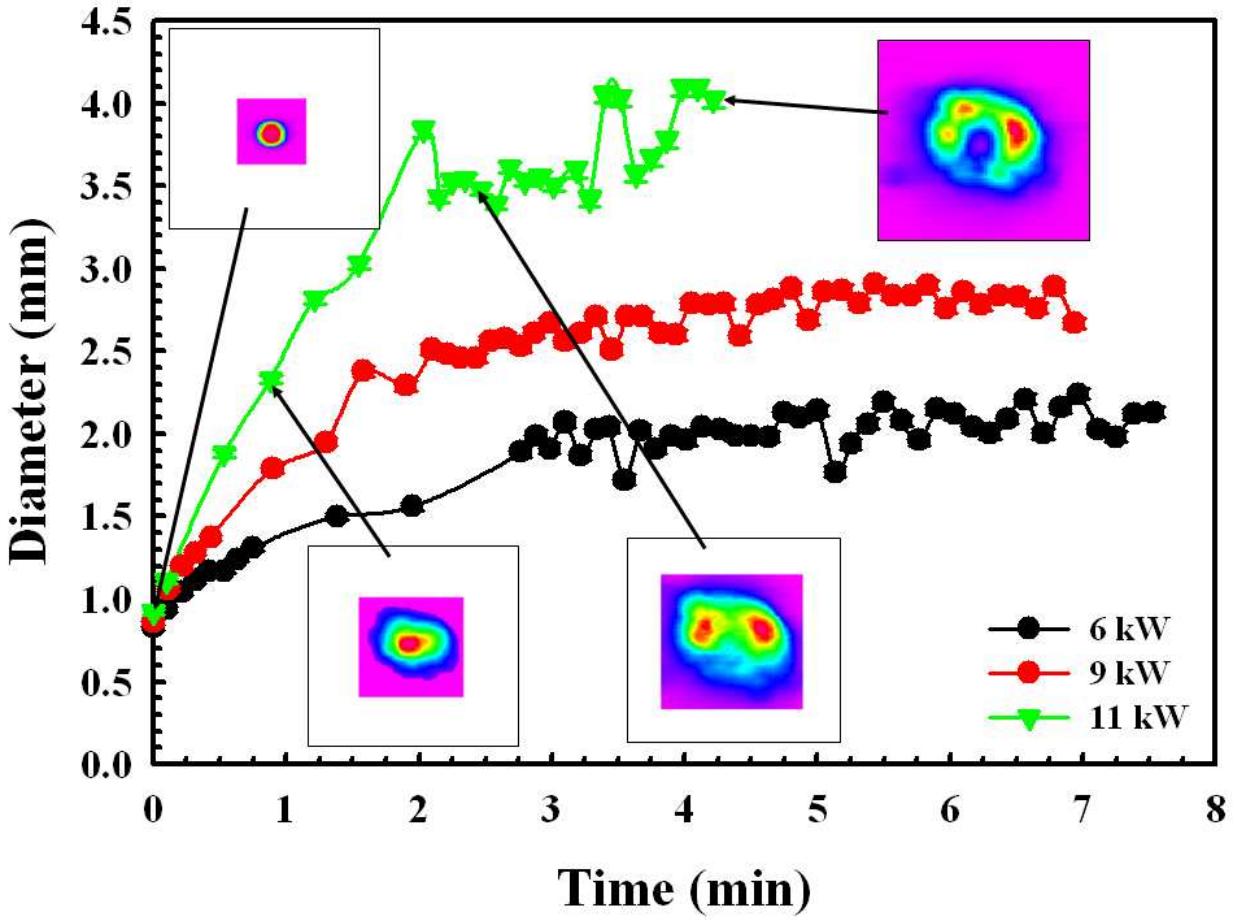

Figure 19: Graph showing measured changes in the beam diameter as a function of time with the damaged collimator and the 500 mm focus length optics at selected powers. Beam profiles obtained at several times at a power of 11kW are also shown.

Characterization of Reflective Optics

Reflective optics transform the beam by redirecting the light off of highly reflective curved surfaces, which collimate and focus the beam. Since the reflective optics are typically manufactured from a conductive metal like copper and are cooled from the inside directly below the exposed surface, these optics may perform much better than transmissive optics at high laser powers. In order to determine if the reflective optics performed better, the collimator and focus optics were characterized in a similar manner to the transmissive optics. The collimator produced a parallel beam that did not change with time.

The Laser Mech® 600 mm focal length reflective optics system was then characterized with the Primes® Focus Monitor. The laser output power does not have a measureable effect on

the beam propagation parameters. Figure 20 shows the beam diameter measurements when the laser was allowed to run continuously. Some of the beam diameters do change more than the resolution, which is 47 µm in this experiment, but no trend is observed that is similar to the transmissive optics trend.

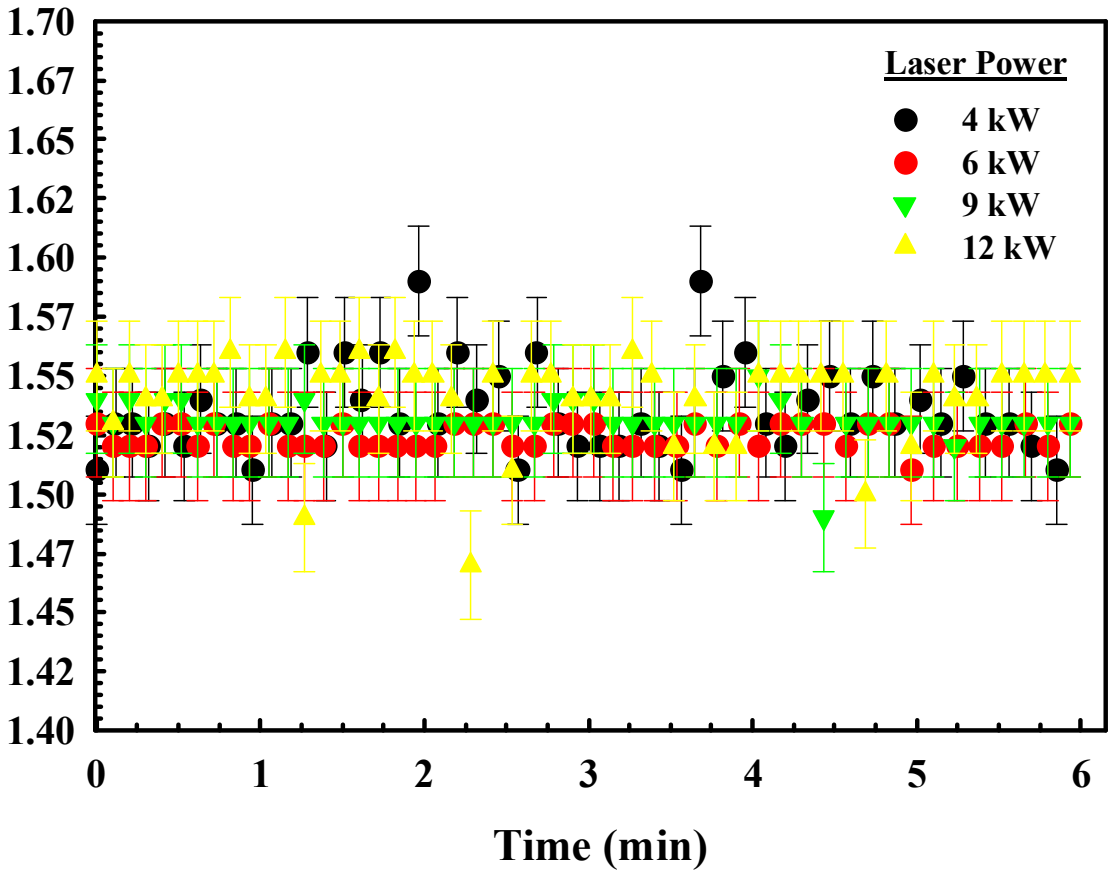

Figure 20: Graph showing the changes in beam diameter at focus during 6 minutes of continuous operation at selected powers with the 600 mm focal length reflective optic configuration.

The relatively large changes can be attributed to the large Rayleigh length (35 mm), or waist, of the reflective optics, which is four times larger than that produced by the transmissive optics. As described earlier, any change in focus length is very sensitive to the difference in focus lens and collimator focal lengths. If the focus length of the Laser Mech® optical assembly was changing, that change should be much larger than the Precitec® optical assembly changes based on the magnitude of the optical magnifications of each optics setup, which is 4.8 for the reflective system and 2.5 for the transmissive system. The Laser Mech® reflective optics provide a very

stable beam over extended operational times for materials processing. No change in beam parameters was detected during any measurements, thus yielding consistent and predictable process quality.

Rapidly Scanning Green (λ = 532 nm) Laser Beam

Molten Pool Geometry

The molten pools that form during laser doping at 2 and 4 m/s and 13.5 W of output power are displayed in Figure 21. The temperature contour is drawn at 1687 K, the melting temperature of silicon, the vectors show the fluid velocity within the pools, and the scale of the axes is in microns.

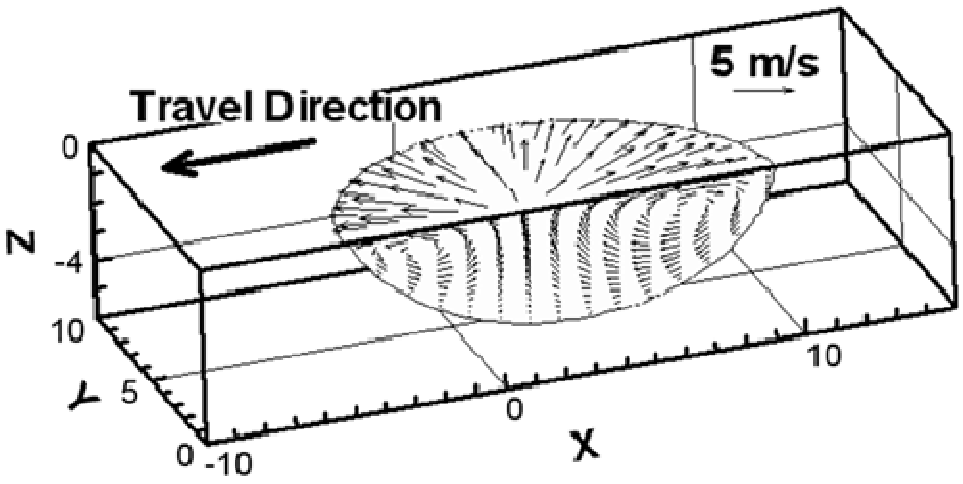

(a)

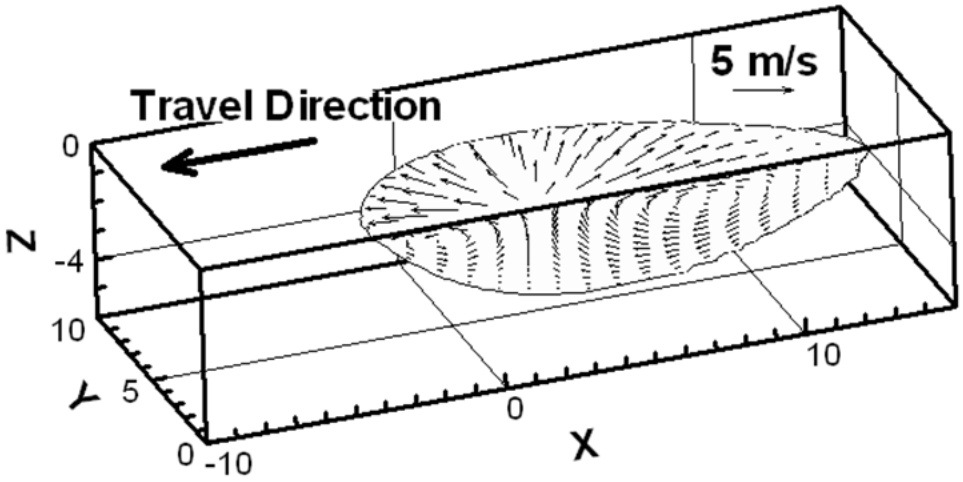

(b)

Figure 21: Molten pool profiles with fluid velocity vectors made with an output power of 13.5 W and travel speeds of (a) 2 m/s and (b) 4 m/s. The axes are in microns and the temperature contour is drawn at 1687 K, the melting temperature of silicon.

The molten pool becomes longer, narrower, and shallower at the higher velocity, which is expected and typical in these types of processes. Additionally, the average fluid velocities decrease at the higher travel speed due to the lower spatial temperature gradients present within the molten pool. From Figure 21, three fluid circulation loops are present within the pool, two in the x-z plane and one in the y-z plane, which is perpendicular to the other two and partially hidden in the figure. These loops will be important in describing some of the dopant distribution profiles later on in this thesis. The relatively high fluid velocities, with maximum velocities on the order of 3 to 4 m/s, leads to a large degree of mixing the dopant into the liquid silicon.

The heat transfer and fluid flow model was validated under several conditions. The experimental and calculated molten pool widths, dopant concentration profiles, and sheet resistances were compared. Figure 22 shows the these two sets of values at 13.5 W output power and beam travel speeds of 2, 4, and 7 m/s. The results show agreement between the experimental and calculated values. The calculated and experimental top surface micrographs are shown in Figure 23. In this figure, the differences in molten pool width appear minimal.

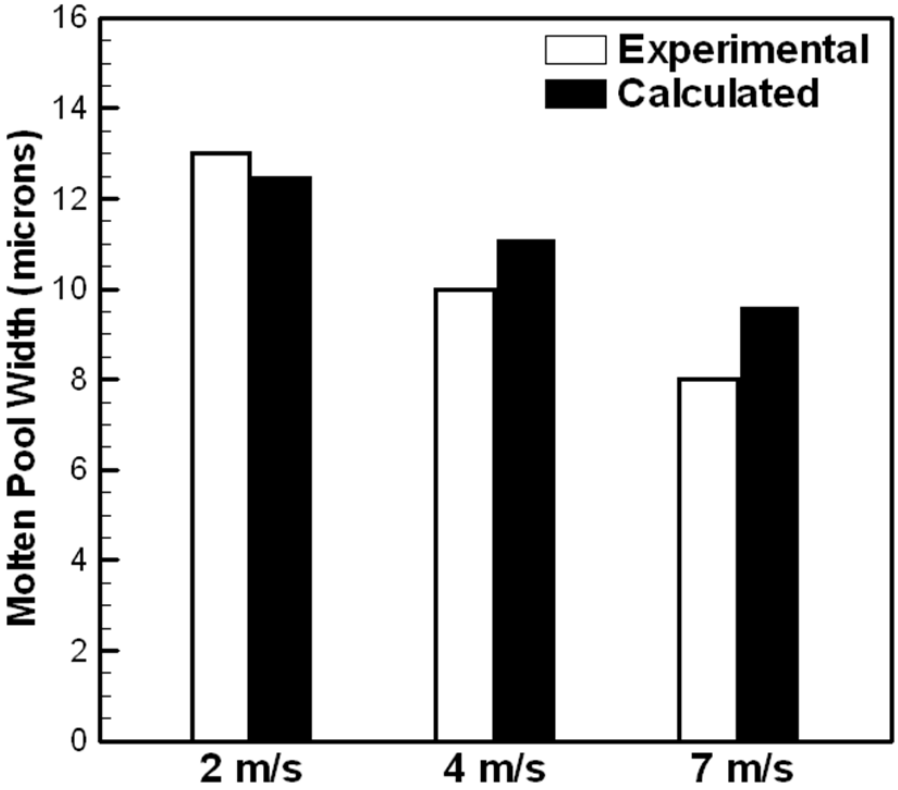

Figure 22: Comparison between the experimental and calculated pool widths shows fair agreement.

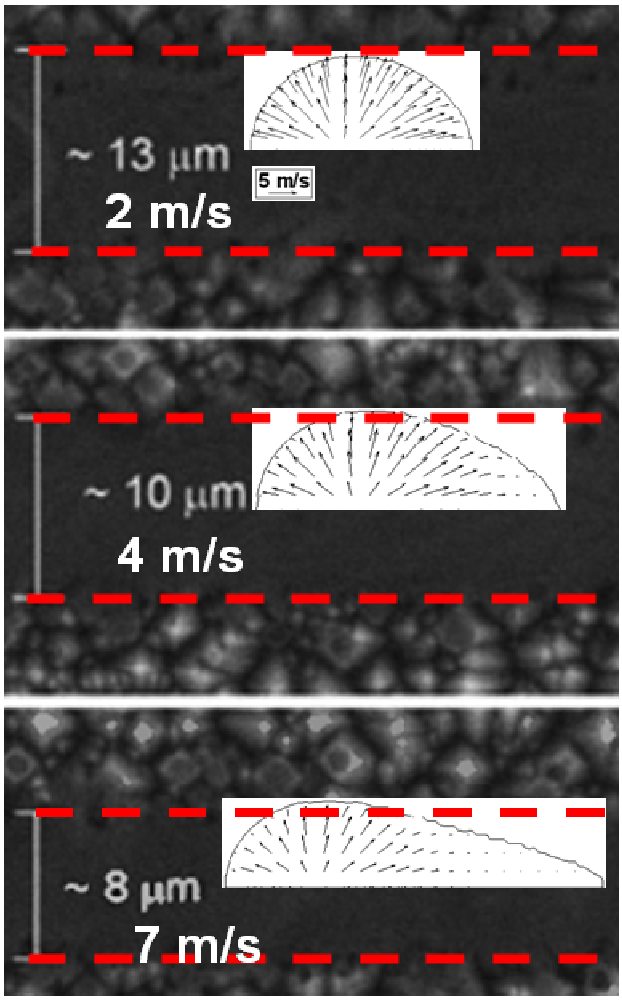

Figure 23: A comparison of the experimental top surface micrographs and calculated velocity fields and melting point contour.

With the validated model, several figures can be constructed that show various important selective emitter characteristics as a function of process parameters. The width and depth of the molten pool define the width and depth of the selective emitter. Shading losses on the front side of the solar cell will be partially determined by the width of the selective emitter because the emitter is plated with metal contacts, which collect charge carries and do not absorb light. The depth determines the dopant depth, which correlates with the some important properties such as sheet resistance and open circuit voltage.

The depth and width of the molten pool are important considerations when determining process parameters for laser doping because both dimensions affect the efficiency of the solar cell. Narrow widths and larger depths are the most desirable for selective emitters. Figure 24 shows a process map for molten pool width in microns with axes of laser power and travel speed

for a 14 μm diameter beam. The two solid lines indicate the limits of the process map at 1687 K, the melting point of silicon, and 3514 K, the silicon boiling temperature.

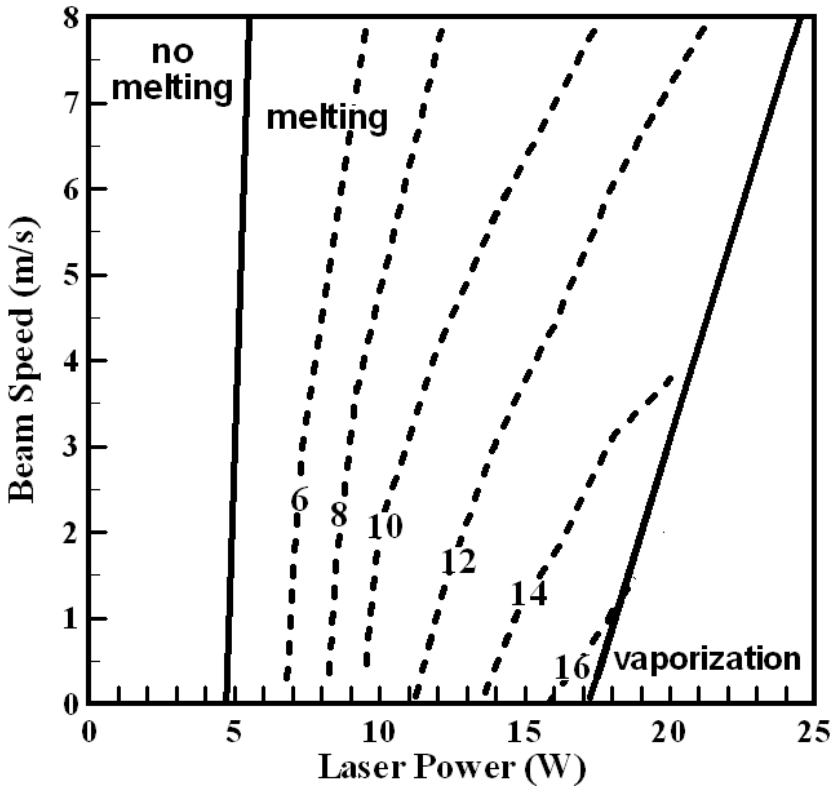

Figure 24: The molten pool width in microns for a 14 um beam as a function of laser power and travel speed shows a range of achievable widths.

The width of the molten region can range from 16 μm to less than 6 μm, so molten pool width can be tuned from slightly greater than the width of the beam to less than half the beam width. Figure 25 shows a process map for the maximum molten pool depth. Achievable depths vary from less than one to greater than six microns. The two process maps show that a minimum width and a maximum depth are not simultaneously achievable for the process parameters shown here. A larger aspect ratio (depth/width) is desirable because deeper depths and narrower widths are the goal. Figure 26 shows the aspect ratio as a function of laser power and travel speed. The highest values occur at higher powers and lower speeds, but there is no maximum value at any point for these process parameters. The aspect ratio at 17 W and 1 m/s is about double compared to 6.5 W and 1 m/s. The aspect ratio is higher at the higher power and lower speed corner of the

map. Some compromise between width and depth will be necessary during the design of process parameters.

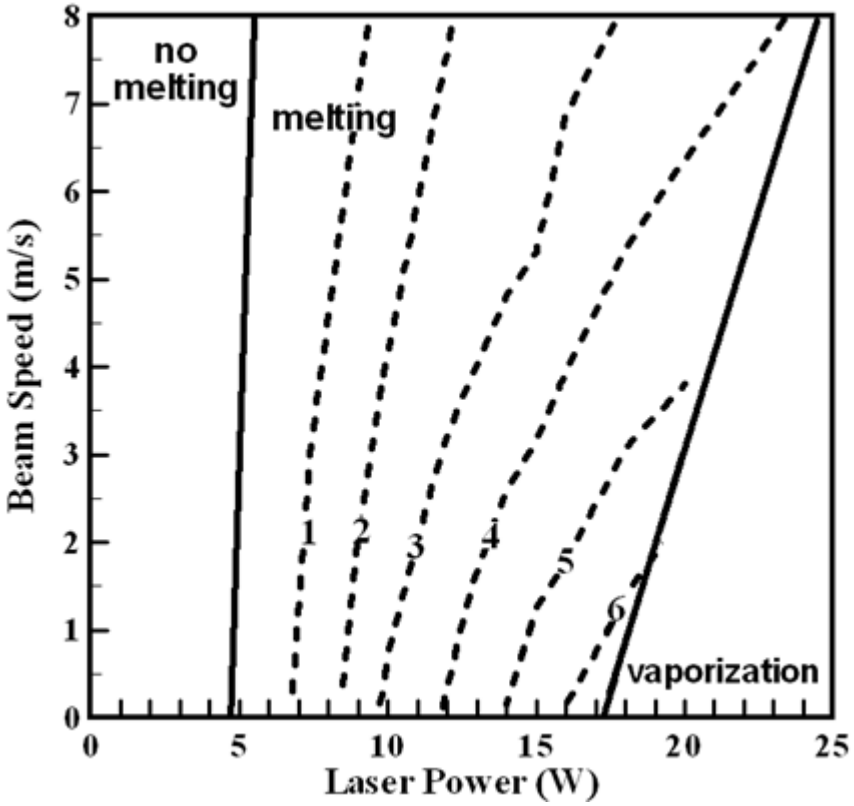

Figure 25: The molten pool depth in microns for a 14 um beam as a function of laser power and travel speed shows a range of achievable depths.

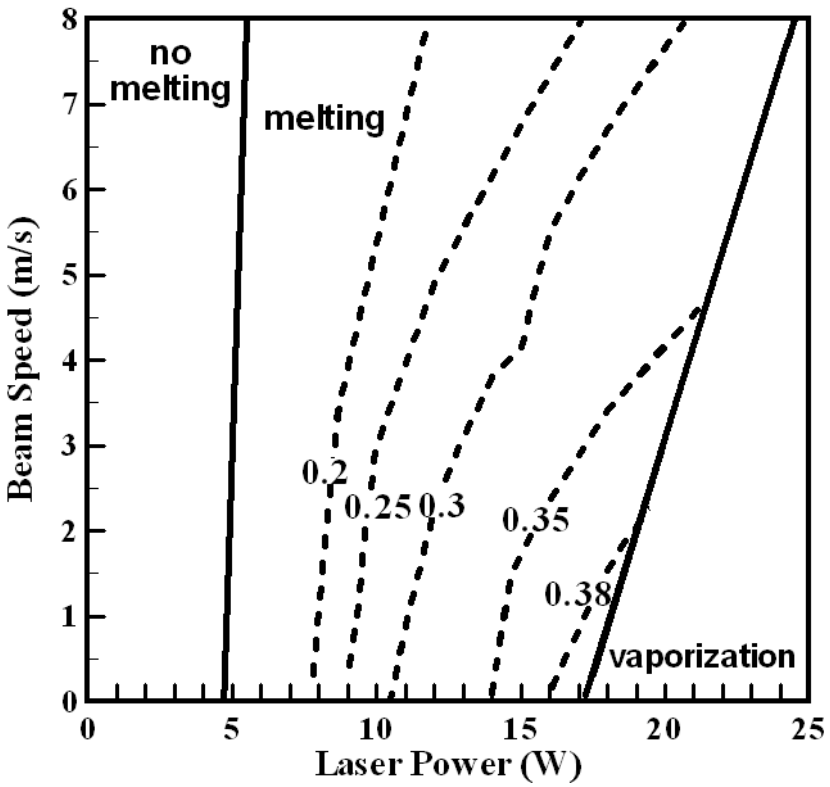

Figure 26: The aspect ratio (depth/width) as a function of power and travel speed does not show a maximum, and the highest values occur at the high power and low speed portion of the map.

Concentration Profile

Fluid velocities play an important role in determining the final dopant distribution profile in the selective emitter. Because the temperature coefficient of surface tension is the main driving force for fluid motion, three main circulation loops are important with one loop orthogonal to the other two. The effect of these loops on the dopant distribution is apparent in Figure 27 and Figure 28, which show the molten pools made with a 15 W beam and select y-z planes of interest at 0.7 and 3.0 m/s, respectively. The phosphorus concentration contour labels are fractions of the surface concentration, 2.7×10^{19} atoms/cm^3.

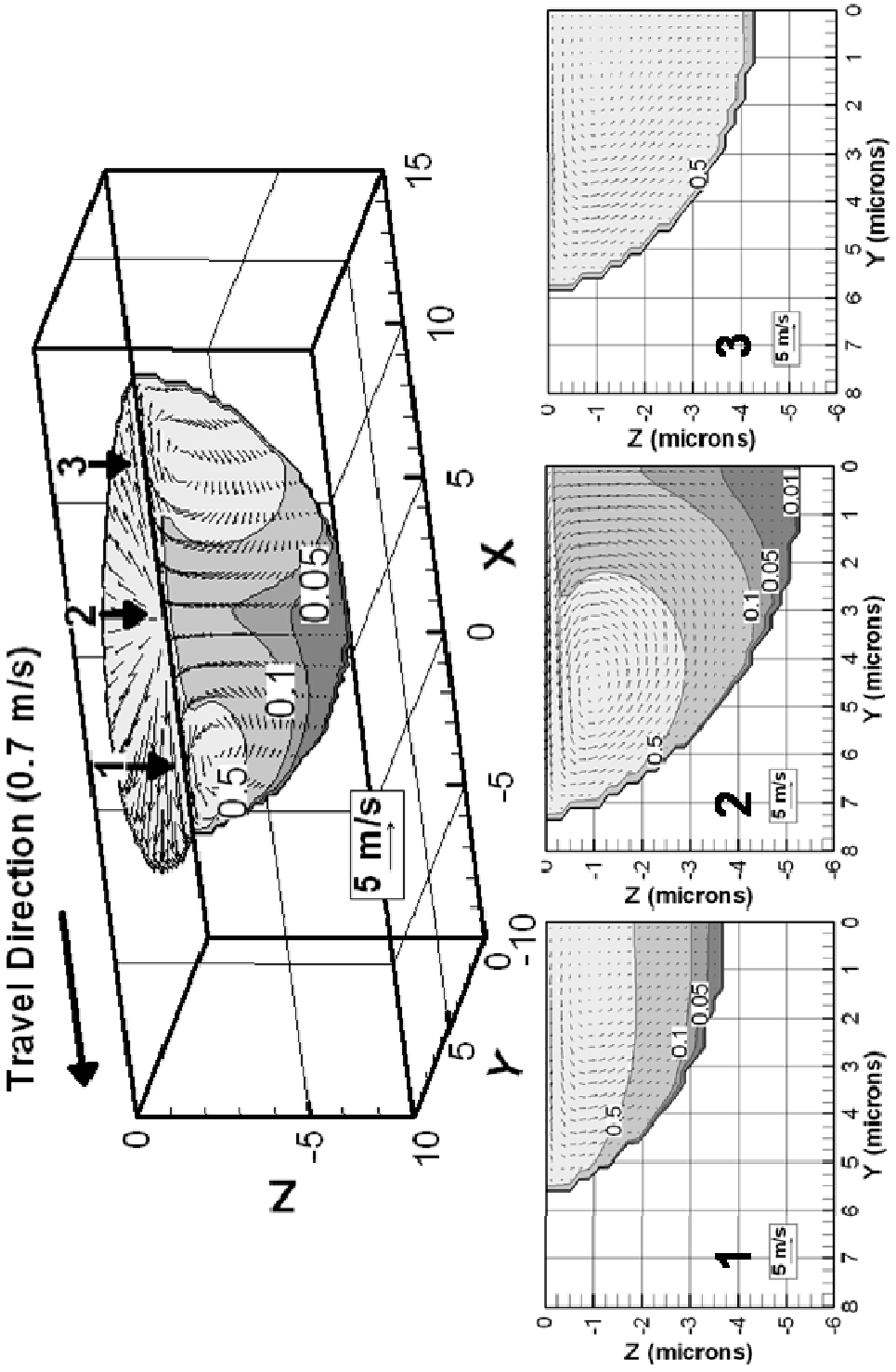

Figure 27: The evolution of the dopant distribution at 15 W and 0.7 m/s is shown. The single planes at the arrows are shown for clarification.

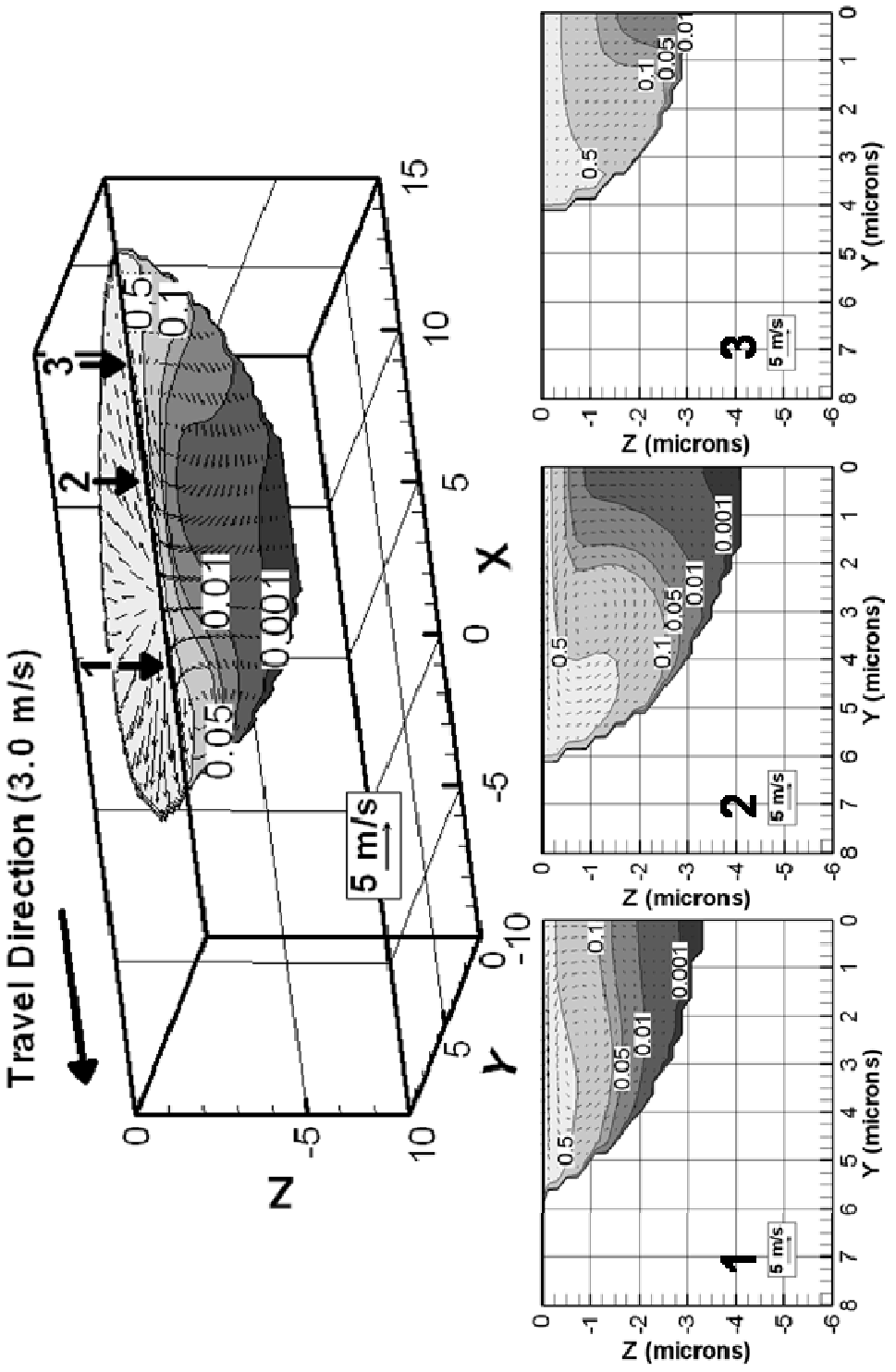

Figure 28: The evolution of the dopant distribution at 15 W and 3.0 m/s is shown. The single planes at the arrows are shown for clarification.

The leading circulation loop in the x-z plane drives the dopant forward and down and does not appear to have much of an effect on the final dopant concentration distribution. The orthogonal loop carries dopant to the outer edge of the molten pool and down to the bottom,

while the second loop in the x-z plane drives dopant to the back of the pool. The final two loops will have the largest impact on the dopant distribution. If the beam travel speed is low as is the case in Figure 27, then the final loop will be the most important because there will be enough time for the dopant to re-distribute itself in a uniform manner, and the effects of the other two loops will not be apparent in the final dopant profile. Depending on the travel speed of the beam, the importance of each loop will vary because at high speeds, the beam will be too fast for fluid motion to have any significant impact, but at lower speeds, complete mixing can occur leading to flat dopant distribution profiles. Fluid motion can also lead to large, instantaneous concentration inhomogeneities within the molten pool. For example at 3.0 m/s in the central plane, the concentration varies by from 0.5 to 0.01 over a 3 μm range at a depth of 1.5 μm. The effect of diffusion can also be observed, especially at the 0.001 contour in Figure 28. This contour is continuously moving deeper into the pool, which implies that fluid motion and diffusion have an equal magnitude as mass transfer mechanisms at that point in the pool.

The experimental and calculated dopant concentration profiles were compared. Figure 29 shows this comparison for a laser power of 15 W and travel speeds of 4 and 6 m/s. The points represent the experimental data, and the dashed lines are the dopant distribution at the center of the molten pool and the maximum concentration at each depth.

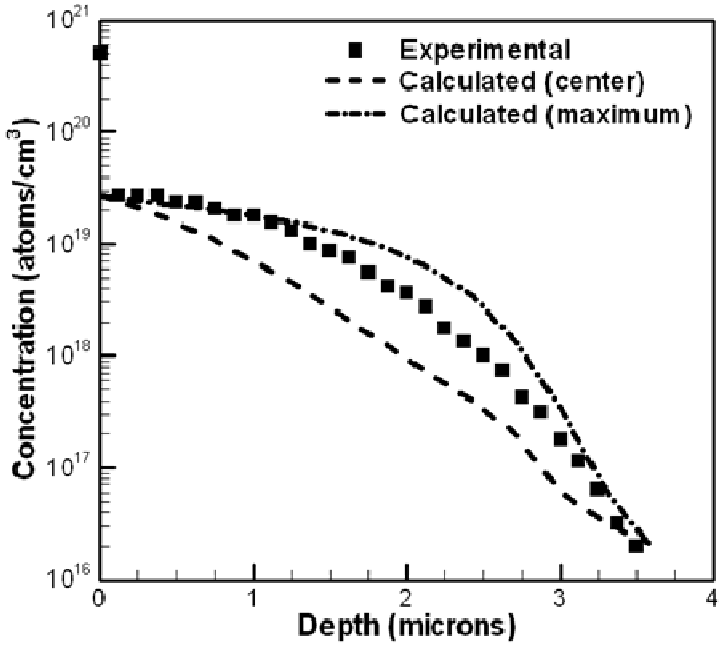

(a)

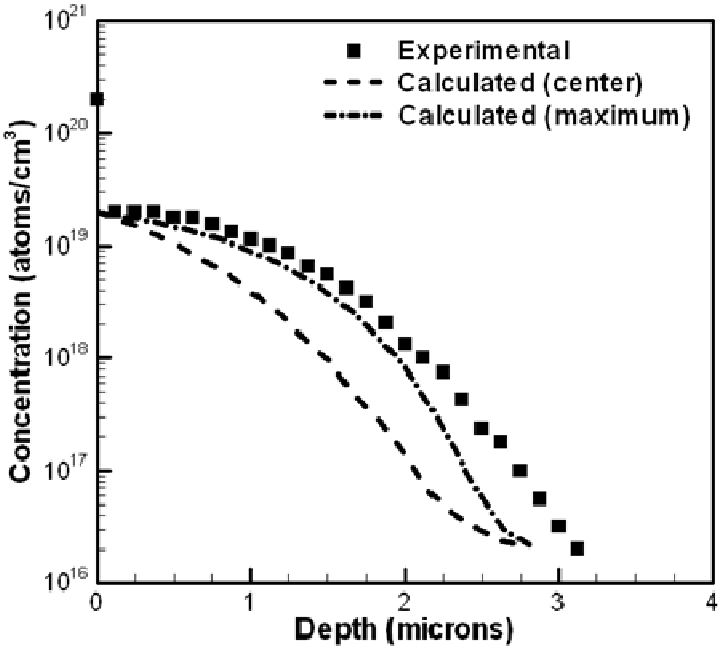

(b)

Figure 29: Agreement between the calculated and experimental phosphorus concentrations for an output power of 15 W and travel speeds of (a) 4 m/s and (b) 6 m/s is good. The second dashed line takes into account poor lateral resolution of the SIMS measurement.

The second dashed line (maximum) is plotted because experimental profile was measured with Secondary Ion Mass Spectroscopy (SIMS), which may be measuring the maximum concentration at each depth if the ion beam size is on the order of the molten pool width [65]. In other words, the lateral resolution of the SIMS measurement is small. Agreement between the experimental and calculated results is good, although the depth is slightly underestimated at 6 m/s. The two dashed lines are not identical because fluid flow enhances mixing and does not allow for homogenous doping at every point in the molten pool. Effects of fluid flow on the final dopant concentration can be readily observed in Figure 30, which shows, for the same set of conditions, the cross-sectional pseudo-single plane with concentration contours as a fraction of the top surface dopant concentration and fluid velocity vectors a plane midway between the points of maximum width and maximum depth.

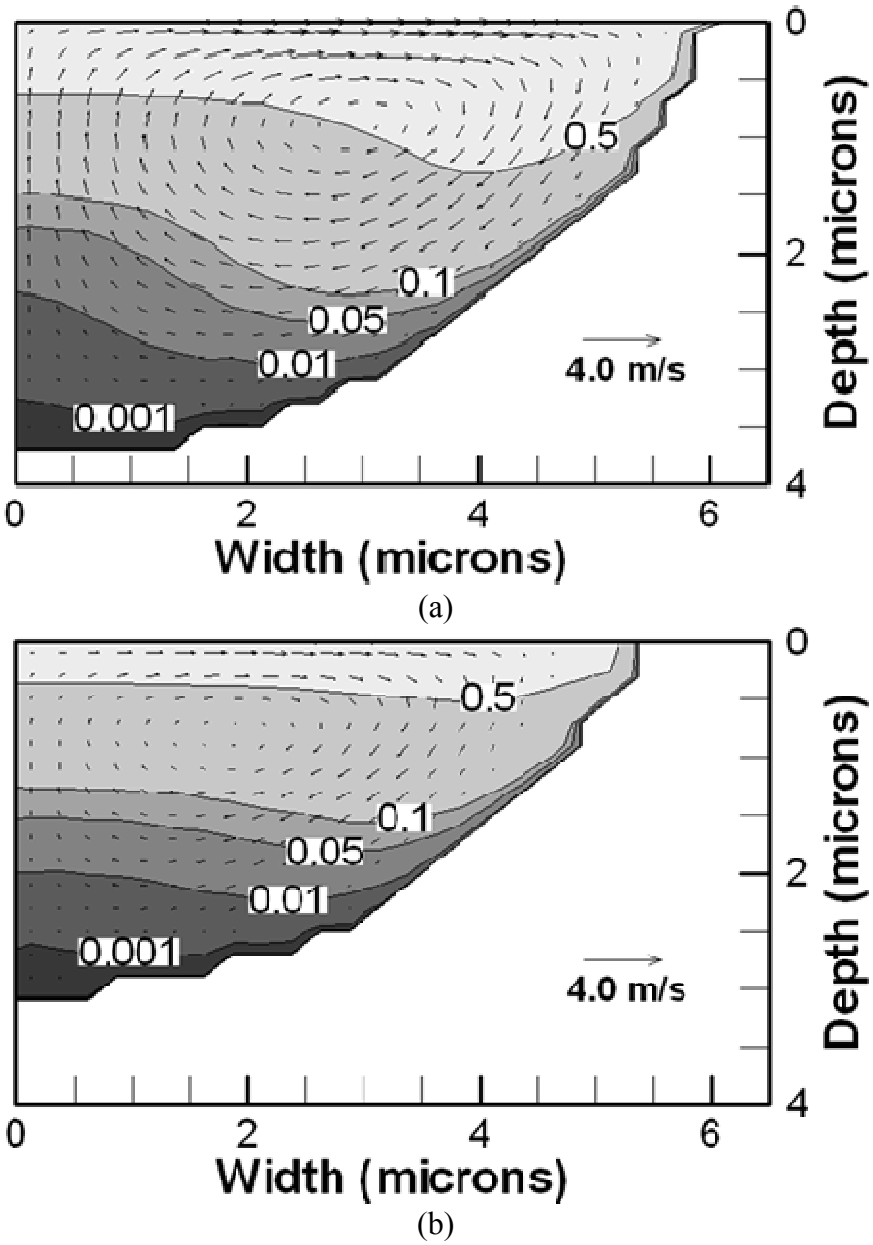

Figure 30: The cross-sectional pseudo-single planes for an output power of 15 W and travel speeds of (a) 4 m/s and (b) 6 m/s show the concentration contours as a fraction of the surface concentration and fluid velocity vectors a plane between the point of maximum width and the point of maximum depth.

The fluid velocities clearly lead to higher dopant concentrations at the wings of the pool and decrease the concentrations at the center. This effect is not as important at 6 m/s travel speed because of the slower fluid velocities and less time available for diffusion. Figure 30 also reveals the dopant concentration inhomogeneities at various depths. For example, for the travel

speed of 4 m/s at a depth of 2.5 μm, the concentration varies by nearly an order of magnitude, from 0.01 to 0.1, across the width of the molten pool.

The final average dopant concentration and the dopant concentration profile shape are easily tunable with process parameters, much in the same way as the molten pool dimensions. The average dopant concentration will have an impact on the conductivity at the interface between the silicon surface and metal contact electrode. The dopant profile shape has not been shown to have an effect on the performance of the selective emitter in service, but this shape takes many forms from uniform to Gaussian and many combinations in between and may be shown to have an effect in the near future. Figure 31 shows the average concentration in atoms/cm^3 as a function of laser power and travel speed.

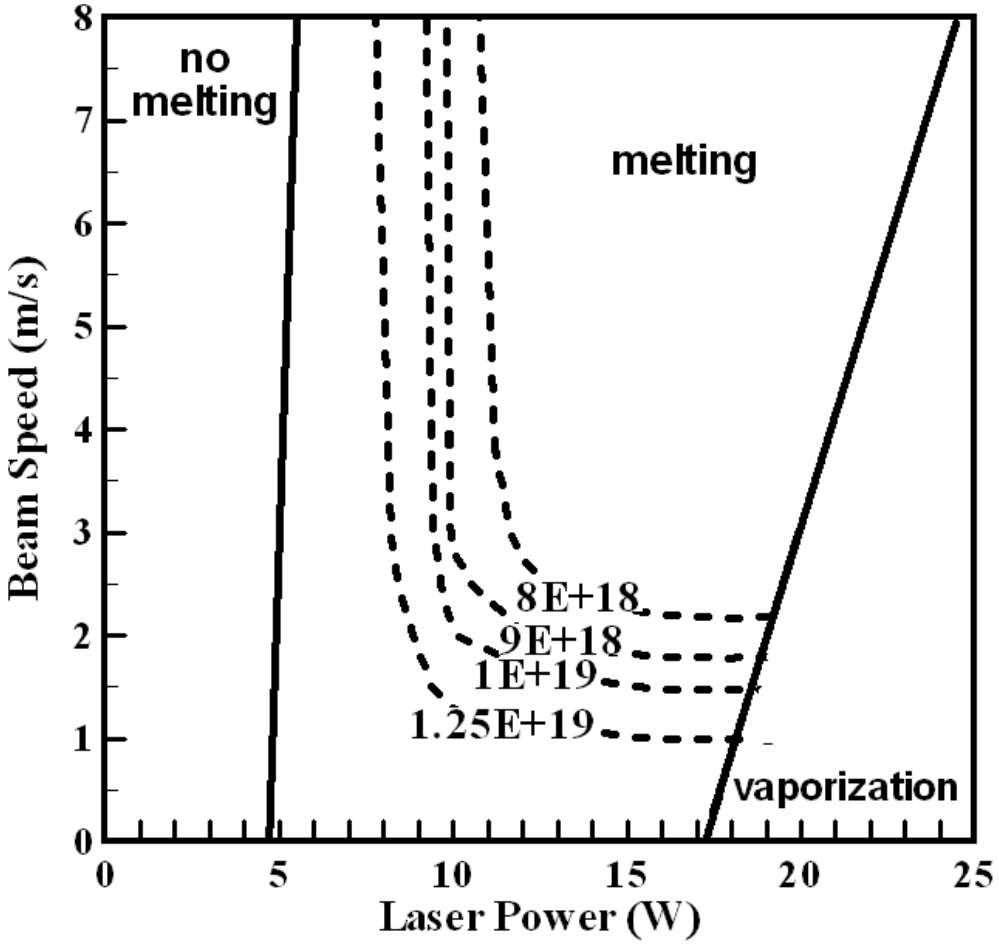

Figure 31: The average concentration of dopant (atoms/cm^3) is shown as function of beam speed and laser power.

The average concentration decreases with increasing speed and power. At higher speeds, there is less time for diffusion, which leads to a lower overall average. With increasing power, the volume of liquid silicon increases, which decreases the average concentration because there is more solvent to dissolve phosphorus. A comparison with the other process maps shows that relatively lower average concentrations are present with higher aspect ratios.

One measure of the dopant concentration profile shape is the degree by which the profile differs from an ideal or given distribution. For these calculations, the profile for a certain set is measured against a perfect uniform dopant profile (i.e. the concentration at every point is equal to the surface concentration, 2.74 x 10^{19} atoms/cm^3). The equation for this profile measurement, which is called the concentration fill factor (FF_c) by [34], is shown below in equation 7. C(z) is the concentration profile, d is the depth of the molten pool along the z axis, w is the width of the molten pool along the y-axis, C_s is the surface concentration, and A_{cs} is the cross-sectional area of the molten pool.

$$FF_C = \frac{\int_0^w \int_0^d C(z)\, dy\, dz}{C_s\, A_{cs}} \tag{8}$$

The maximum is 1.0 and the minimum is 0.00073 if there is no diffusion. Figure 32 shows the FF_c as a function of output power and travel speed. The maximum for these parameters occurs at lower speeds and lower powers. Higher values of FF_c imply more homogeneous and uniform dopant concentration profiles, so higher average dopant concentrations and more uniform profiles are common at lower powers and speeds. The opposite is true at higher powers and higher speeds, where the concentrations are more Gaussian, and the average concentrations are lower.

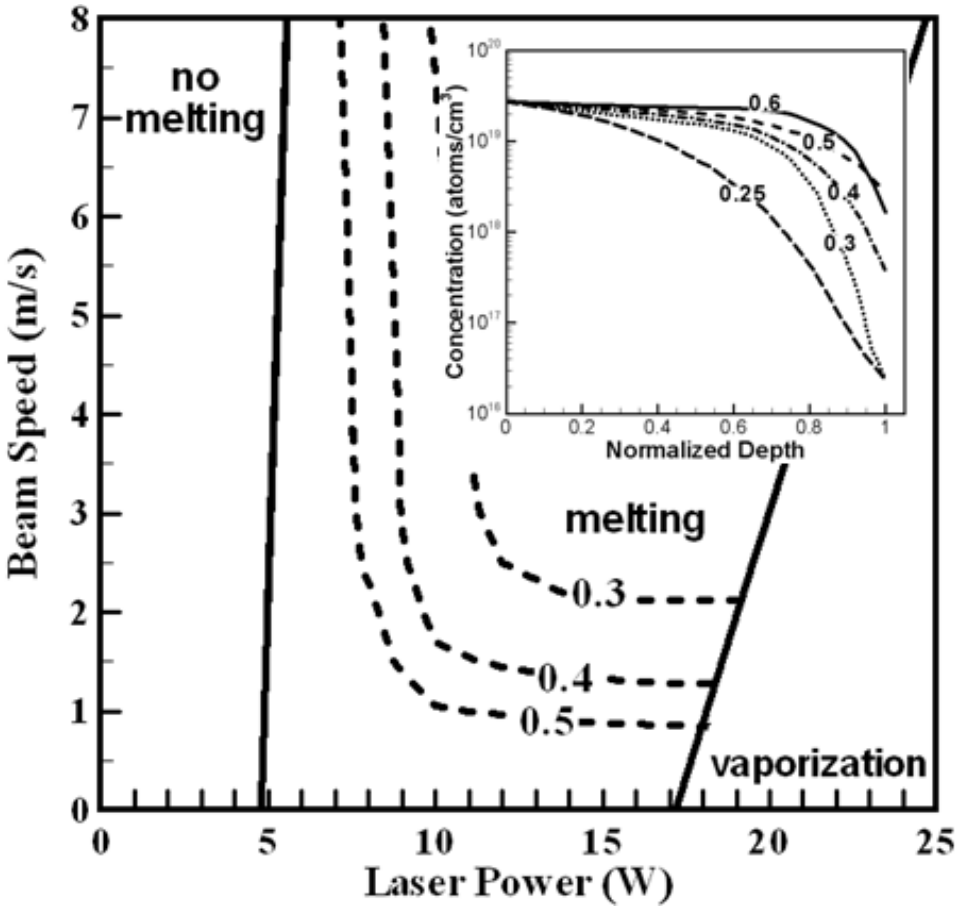

Figure 32: A measure (FF_c) of the dopant concentration profile shape is shown as a function of laser power and travel speed.

Dimensionless Analysis

There are two mass transfer mechanisms, diffusion and convection. Diffusion is caused by a concentration gradient and occurs through the random movement of atoms. Convection results from the bulk motion of the fluid. Many times the dimensionless Peclet number is used to determine which mechanism is dominant. The Peclet number is determined as:

$$Pe = \frac{U\,L}{D} = \frac{(v_{\max}/4)(w/2)}{D} \qquad (9)$$

where U is the characteristic velocity of the fluid, L is the characteristic length that the fluid has to travel, D is the diffusion coefficient, v_{max} is the maximum velocity at the top of the molten pool in the y-axis direction, and w is the width of the pool. Twenty-five percent of the v_{max} is taken as the characteristic velocity because that value is close to the average velocity in the y-direction at the top surface. The half-width of the molten pool is taken as the characteristic

length. If the Peclet number is greater than 10, then convection is the dominant mass transfer mechanism, and diffusion can be ignored. At values less than 0.1, diffusion is much more important than convection. At intermediate values, both mechanisms are significant. Figure 33 shows the Peclet number as a function of travel speed at various powers. In almost every case, the Peclet number exceeds 10, which indicates convection is the dominant mass transfer mechanism. The values decrease with speed because the pool dimensions and fluid velocities decrease with speed. With increasing power, both the width of molten pool and the fluid velocities increase, which increases the Peclet number.

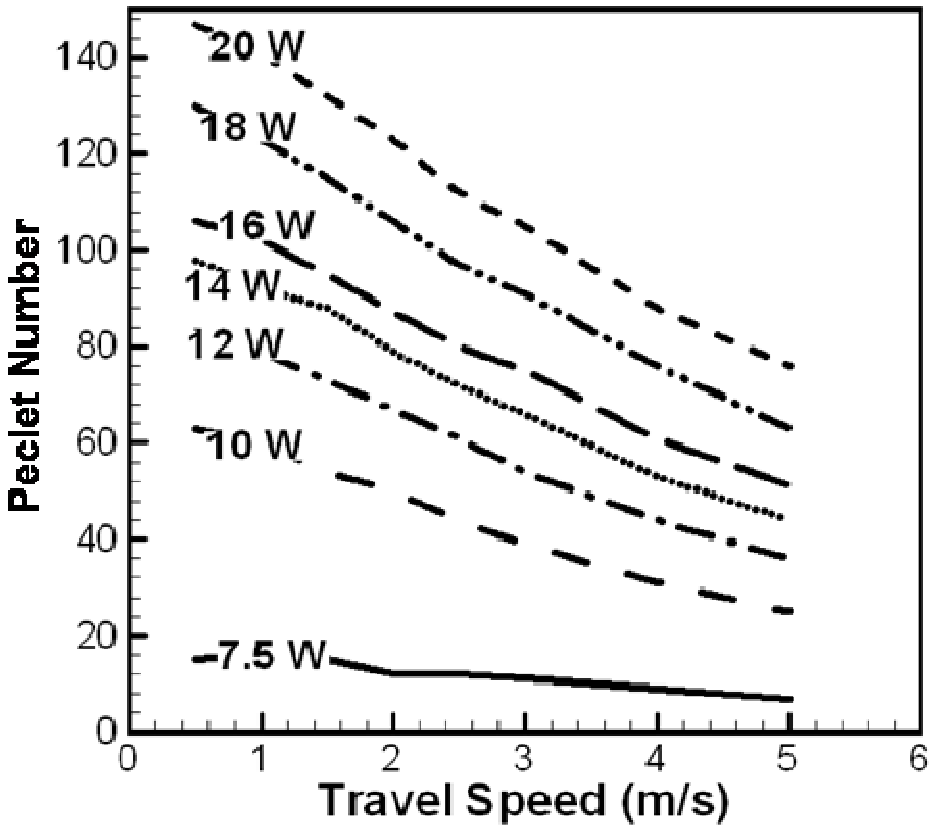

Figure 33: The dimensionless Pelcet number decreases with travel speed and increases with output power. Relatively high Peclet numbers indicate convection is the dominant mass transfer mechanism.

Because the fluid velocities are relatively high and convection is the dominant mass transfer mechanism, one may expect the pool to be well mixed, with the dopant concentration everywhere in the molten pool not less 50% of the surface concentration. If the fluid has time to go from the center of the pool to the edge ten times, then the pool should be well mixed. The

amount of available time is the length of the pool divided by travel speed. The ratio of time for ten cycles to available time is a good indicator of whether the pool will be well-mixed. This ratio is greater than one for all cases examined here and greater than 5 for the majority of cases. Since the ratio is greater than one, there will not be enough time for the fluid to cycle and the pool to become well mixed.

Sheet Resistance

Sheet resistance is a common measure of the quality of the highly doped region of the selective emitter. After laser doping, resistance in the former molten region should drop since more dopant atoms have been introduced. Values below 30 ohms/square are considered acceptable [28]. Sheet resistance is determined using an empirical formula [36]:

$$R_{sh} = \frac{1}{q\int_0^d C(z)\,\mu(z)\,dz} \tag{10}$$

where q is the charge of an electron and μ(z) is the electron mobility, which is a function of the concentration profile [37]:

$$\mu(z) = \mu_{\min} + \frac{\mu_{\max} - \mu_{\min}}{1 + \left(C(z)/C_{sub}\right)^{\alpha}} \tag{11}$$

μ_{min}, μ_{max}, and α are fitted values of 130 cm^2/V-s, 500 cm^2/V-s, and 1.25, respectively. C_{sub} is the background concentration of the substrate, 2.0 x 10^{16} atoms/cm^3. With the validated concentration profiles, the sheet resistance values can also be validated. Figure 34 is a comparison between the calculated and experimental sheet resistances at various travel speeds and an output power of 15 W. The two sets of values show good agreement. The up C values are determined from the maximum concentration at each depth, while the down C values are determined by the concentration profile at the center of the molten pool.

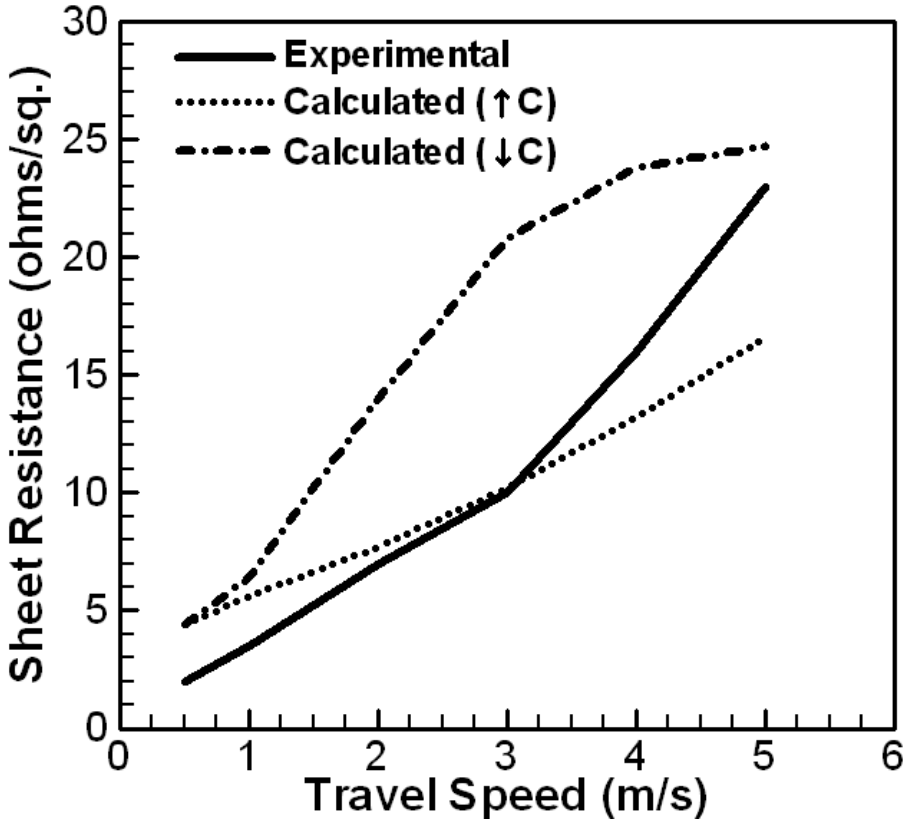

Figure 34: A comparison between calculated and experimental values of sheet resistance shows good agreement. The up arrow concentration is the maximum concentration at each depth. The down arrow indicates the concentration at the middle of the cross section.

With a calculated dopant concentration profile and the empirical relations, the sheet resistance values were calculated for a range of process parameters and are shown in Figure 35 with units of ohms/square.

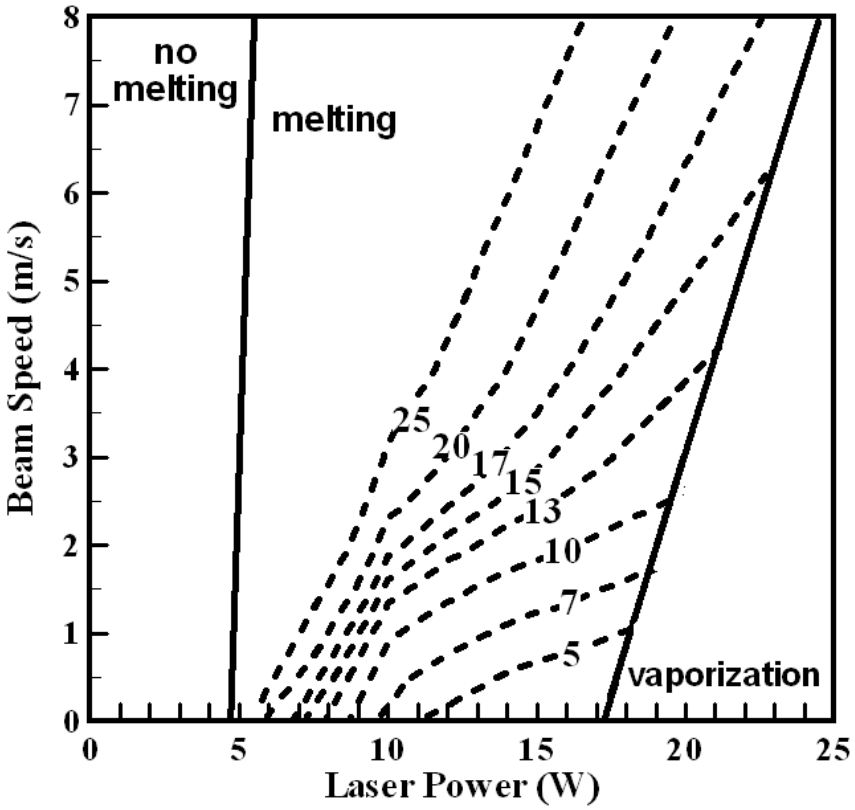

Figure 35: Calculate sheet resistance values in ohms/square are shown as function of laser power and travel speed.

Lower travel speeds and higher powers produce the lowest resistances because there is more dopant, in absolute terms, within the molten pool, which makes the selective emitter more conductive. If this process map is compared with the dopant concentration profile map, lower resistance values are associated with more uniform profiles. These results agree well with the literature, which suggests that deeper depths produce lower sheet resistances.

Chapter 5: Summary and Conclusions

The use of a mathematical model that solves the equations for conservation of mass, momentum, and energy has been applied to the formation of a selective emitter with the laser doping process. Due to the geometry of the sample in terms of surface layers, modifications to the model that account for the heating and melting of these layers have been made. With experimental molten pool widths, dopant distribution profiles, and sheet resistance values the model has been validated. Five selective emitter characteristics have been investigated as a function of process parameters, and all five have been presented in the form of process maps with axes of output power and travel speed. The major findings of this work are expressed below.

- The molten pool geometry and dopant concentration profile under laser doping conditions has been predicted and validated with independent experimental data.
- Process maps for the molten pool geometry, concentration profile characteristics, and sheet resistance were developed.
- The maps show that desirable selective emitter properties (narrower widths and deeper depths) are not achieved simultaneously. A high aspect ratio and low sheet resistances are achieved at lower speeds (< 2 m/s) and higher powers (> 14 W).
- The volume average dopant concentrations are sensitive to speed at higher powers, and at lower powers show little change with speed.
- Dimensionless Peclet number calculations show that convection dominates mass transfer.
- Low sheet resistance values (5 ohms) are obtained at high powers and low travel speeds.

Chapter 6: Future Work

The work presented in this thesis described how numerical modeling can be applied to the laser doping process in order to predict selective emitter geometry and properties. Future work should investigate how silicon material defects (dislocations, vacancies, and interstitials) affect the performance of photovoltaic devices. These defects should then be tied to certain conditions during processing such as spatial temperature gradients, thermal cycles, and solidification rates that can be easily calculated with a heat transfer and fluid flow model. This thesis and other work have proven the utility of numerical modeling to laser processing of silicon. With reliable process-properties-performance relationships, numerical modeling can fully capture laser processing of silicon and provide insights and into current processes and future processes. This work will not necessarily be easy because it will require micro/nano-characterization techniques such as transmission electron microscopy to be related to macro-scale properties. This additional work could also be transferred to other material systems where laser processing at the micron scale is necessary.

References

1. “High Power Fiber Lasers for Industrial Applications.” Accessed May 10, 2010. http://www.ipgphotonics.com/Collateral/Documents/English-US/HP_Brochure.pdf.

2. “Fluoride Crystal Materials: Corning® Calcium Fluoride (CaF2) – Code 9575.” Accessed March 21, 2011. http://www.corning.com/WorkArea/downloadasset.aspx?id=34271.

3. Reitemeyer, D., Seefeld, T., and Vollersten, F. 2010. Online focus shift measurement in high power fiber laser welding. *Proc. 29th ICALEO*. eds. X. Liu, K. Loffler, and K. Washio, pp. 13-20.

4. Havrilla, D., Holzer, M., and Olschowsky, P. 2010. Latest research results with high power solid state laser optics with minimized focus shift. *Proc. 29th ICALEO*. eds. X. Liu, K. Loffler, and K. Washio, pp. 29-32.

5. Klein, C.A., 2007. Materials for high-energy laser windows: how thermal lensing and thermal stresses control the performance. *Proceedings of Optical Materials and Structures Technologies III*. eds. W.A. Goodman and J.L. Robichaud, pp. 1-19. Proc. of SPIE.

6. Blomster, O., Palsson, M., Roos, S.O., Blomqvist, M., Abt, F., Dausinger, F., Deininger, C., and Huonker, M. 2008. Optics performance at high-power levels. *Proceedings of Solid State Lasers XVII: Technology and Devices*. eds. W.A. Clarkson, N. Hodgson, R.K. Shori, pp. 1-10. Proc. of SPIE.

7. Abt, F., Heb, A., and Dausinger, F. May 2008. Focusing high-power, single-mode laser beams. *Photonics Spectra*.

8. Bosman, A. J. and Havinga, E. E. 1962. Temperature dependence of dielectric constants of cubic ionic materials. *Physical Review*. 129 (4): 1593-1600.

9. Leviton, D. B. and Frey, B. J. 2006. Temperature-dependent bbsolute refractive index measurements of synthetic fused silica. *Proceedings of Optomechanical Technologies for Astronomy*. eds. E. Atad-Ettedgui, J. Antebi, and D. Lemke, pp. 1-11. Proc. of SPIE.

10. Riza, N. A. and Mughal, M. J. 2003. The NU-POWER all-digital beam profiler: a powerful new tool for spatially characterizing laser beams. *Proceedings of Applications of Photonic Technology 6*. eds. R. A. Lessard and G. A. Lampropoulos, pp. 87-95. Proc. of SPIE.

11. “MicroSpotMonitor Data Sheet.” Accessed June 15, 2011. http://www.primes.de/download/produkte/f3_11_Datasheet_MSM_HP_MSM_low.pdf.

12. Pilcher, M. L. and Tozer, B. A. 1966. Determination of laser beam energy profile by a multi-layer foil technique. *British Journal of Applied Physics* 17 (695): 695-697.

13. Bahk, S. W., Rousseau, P., Planchon, T. A., Chvykov, V., Kalintchenko, G., Maksimchuk, A., Mourou, G. A., and Yanovsky, V. 2004. generation and characterization of the highest laser intensities (10^{22} W/cm^2). *Optics Letters* 29 (24): 2837-2839.

14. Shrivasta, B. B., Benerji, N. S., Bhatnagar, P., Vora, H. S., and Nundy, U. 2004. Development of automated ultraviolet laser beam profiling system using fluorometric technique. *Proceedings of International Conference in Photonics*. pp. 64-69.

15. Ciofini, M., Lapucci, A., Lolli, S. 2003. Diffractive optical components for high power laser beam sampling. *Journal of Optics A: Pure and Applied Optics* 5 (186): 186-191.

16. Nishioka, N. S., Bua, D. P., and Deutsch, T. F. 1987. Measurement of a laser-beam profile by using a video camera. *Lasers in Medical Science* 2 (21): 1-3.

17. Rose, A., Nie, Y. X., and Gupta, R. 1986. Laser beam profile measurement by photothermal deflection technique. *Applied Optics* 25 (11): 1738-1741.

18. Mallidi, S. and Emelianov, S. 2009. Photoacoustic technique to measure beam profile of pulsed laser systems. *Review of Scientific Instruments* 80 (5): 1-5.

19. Li, Q., Lei, H., and Zuo, T. 2000 Research on high power laser beam and focus transverse intensity distribution measuring instrument. *Proceedings of Instruments for Optics and Optoelectronic Inspection and Control*. eds. G. H. Wei and S. Liu, pp. 45-49. Proc. of SPIE.

20. Gilse, J. V., Koczera, S., and Greby, D. 1991. Direct laser beam diagnostics. *Proceedings of Laser Beam Diagnostics*. eds. R. N. Hindy and Y. Kohanzadeh, pp. 45-54. Proc. of SPIE.

21. European Photovoltaic Industry Association. 2011. Solar photovoltaics competing in the energy sector – on the road to competitiveness.

22. Hedrick, B.L. 2011. Masters Thesis, Characterization of laser fired contacts, laser doped emitters, and fixed charge passivation for improved silicon solar cells. The Pennsylvania State University.

23. Mouhoub, A., Benhahia, B., Mahoudi, B., and Mougas, A. 2003. Selective emitters for screen printed multicrystalline silicon solar cells. International Congress of Photovoltaic and Wind Energy. Tlemcen, Algeria. December 2003.

24. Ruby, D. S., Yang, P., Roy M., and Narayanan, S. 1997. Recent progress on the self-aligned, selective-emitter silicon solar cell. 26th IEEE Photovoltaic Specialists Conference. Anaheim, California. October 1997.

25. Pirozzi, L., Arabito, G., Artuso, F., Barbarossa, V., Besi-Vetrella, U., Loreti, S., Mangiapane, P., and Salza, E. 2001. Selective emitters in buried contact silicon solar cells: some low-cost solutions. Solar Energy Materials & Solar Cells, 65: 287-295.

26. Lin, C. H., Hsu, S. P., Liou, J. J., Chuang, C. P., Lu, W. H., Chang, W. L. 2010. Characterization of selective-emitter solar cells consists of laser opened window and subsequently screen-printed electrodes. 35th IEEE Photovoltaic Specialists Conference. Honolulu, Hawaii. June 2010.

27. Tjahjono, B. S., Guo, J. H., Hameiri, L., Mai, L., Sugianto, A., Wang, S., and Wenham, S.R. 2007. High efficiency solar cell structures through the use of laser doping. 22nd European Photovoltaic Solar Energy Conference. September 2007. Milan, Italy.

28. Sugianto, A., Bovatsek, J., Wenham, S., Tjahjono, B., Xu, G., Yao, Y., Hallam, B., Bai, X., Kuepper, N., Chong, C. M., and Patel, R. 2010. 18.5% Laser-doped solar cell on cz p-type silicon. 35th IEEE Photovoltaic Specialists Conference. June 2010. Honolulu, Hawaii.

29. Kohler, J.R., Grabitz, P., Eisele, S.J., Roder, T.C., and Werner, J.H. 2009. Laser doped selective emitters yield 0.5% efficiency gain. 24th EU PVSEC Proceedings 2009. 1847-1850.

30. Schulz-Ruhtenberg, M., Haeberle, A., Russell, R., Hernandez, J. R., and Krantz, S. 2011. Influence of the pulse width for visible pulsed laser doping for crystalline solar cells using phosphosilicate glass. Journal of Laser Micro/Nanoengineering, 6 (1):64-68.

31. Paviet-Salomon, B., Gall, S., Monna, R., Manuel, S., and Slaoui, A. 2011. Experimental and analytical study of saturation current density of laser doped phosphorus emitters for silicon solar cells. Solar Energy Materials & Solar Cells, 95: 2536-2539.

32. Jager, U., Mack, S., Kimmerle, A., Wolf, A., and Preu, R. 2010. Influence of doping profile of highly doped regions for selective emitter solar cells. 35th IEEE Photovoltaic Specialists Conference. Honolulu, HI.

33. Jager, U., Thaidigsmann, B., Okanovic, M., and Preu, R. 2011. Quantum efficiency analysis of highly doped areas for selective emitter solar cells. Energy Procedia, 8: 193-199.

34. Kohler, J. R. and Eisele, S. 2010. Influence of precursor layer ablation on laser doping of silicon. Progress in Photovoltaics: Research and Applications, 18: 334-339.

35. Hirata, K., Ogane, A., Saitoh, T., Kitiyanan, A., Sugimura, E., and Fuyuki, T. 2009. Optimization of cw laser doping in crystalline silicon solar cell fabrication process. 24th European Photovoltaic Solar Energy Conference. September 2009. Hamburg, Germany.

36. Wen, Z., Zhou, C., and Wang, W. 2011. Co-optimization of emitter profile and metal grid of selective emitter silicon solar cells. Progress in Photovoltaics: Research and Applications. DOI: 10.1002/pip.1142

37. Klaassen, D.B.M., Slotboom, J.W., and DeGraaff, H.C. 1992. Unified apparent bandgap narrowing in n-type and p-type silicon. Solid State Electronics, 35 (2) 125-129.

38. Poulain, G., Blanc, D., Semmache, B., Pellegrin, Y., and Lemiti, M. 2011. Finite element simulation of laser-induced diffusion in silicon. Energy Procedia 8: 587-591.

39. Hecht, E. 2002. *Optics, 4th Edition.* p. 163 , New York, N. Y., Addison Wesley

40. "Focus Monitor/Beam Monitor and Laser Diagnose Software 2.73: User's Manual and Documentation." Accessed April 1, 2011, http://primes.de/download/support/f49_ManualFocusMonitorApril2007-WEB.pdf.

41. Porras, M. and Medina, R. 1995. Entropy-based Definition of Laser Beam Diameter. *Applied Optics* 34 (36): 8247-8251.

42. "Lasers and Laser-Related Equipment – Test Methods for Laser Beam Widths, Divergence Angles, and Beam Propagation Ratios," ISO 11146:2005.

43. Khan, P. A. A. and DebRoy, T. 1984. Alloying element vaporization and weld pool temperature during laser welding of AISI 202 Stainless Steel. Metallurgical Transactions B, 15B, 641-644.

44. Collur, M. M., Paul, A., and DebRoy, T. 1987. Mechanism of alloying element vaporization during laser welding. Metallurgical Transactions B, 18B, 734-740.

45. Paul, A. and DebRoy, T. 1988. Free surface flow and heat transfer in conduction mode laser welding. Metallurgical Transactions B, 19B, 851-858.

46. Mundra, K. and DebRoy, T. 1993. Calculation of weld metal composition change in high-power conduction mode carbon dioxide laser-welded stainless steels. Metallurgical Transactions B, 24B, 145-155.

47. Hong, T., DebRoy, T., Babu, S. S., and David, S. A. 2000. Modeling of inclusion growth and dissolution in the weld pool. Metallurgical Transactions B, 31B, 161-169.

48. Zhao, H. and DebRoy, T. 2001. Weld metal composition change during conduction mode laser welding of aluminum alloy 5182. Metallurgical Transactions B, 32B, 163-172.
49. Pitscheneder, W., Ebner, R., Hong, T., DebRoy, T., Mundra, K., and Benes, R. 1998. Experimental and numerical investigation of transport phenomenon in conduction mode weld pools. Mathematical Modelling of Weld Phenomena 4. Editor H. Cerjak and
50. S. V. Patankar, Numerical Heat Transfer and Fluid Flow (Hemisphere, New York, 1980).
51. Thyagarajan, K. and Ghatak, A. 2010. Lasers: Fundamentals and Applications. 2nd Edition. Springer. New York, NY.
52. Raghavan, A., Palmer, T.A., and DebRoy, T., "Evolution of Laser Fired Aluminum-Silicon Contact Geometry in Photovoltaic Devices", Journal of Applied Physics, 111, 02493, 2012, doi: 10.1063/1.3675442.
53. Smithells Metals Reference Book, 7th Edition, 1992
54. Kawamura, H., Fukuyama, H., Watanabe, M., and Hibiya, T 2005. Normal spectral emissivity of undercooled liquid silicon. Measurement and Science and Technology, 16: 386-393.
55. W.K. Rhim and K. Ohsaka, J. Crystal Growth 208, 313-321 (2000)
56. A. De, T. DebRoy, Sci. Tech. Weld. and Joining 11 (2), 143-144 (2006)
57. A. De, T. DebRoy, J. Appl. Phys 95 (9), 5230-5240 (2004)
58. J.L. Murray, A.J. McCalister, Bulletin of Alloy Phase Diagrams 5 (1), 74-84 (1984)
59. L.B. Pakratz, Thermodynamic Properties of Elements and Oxides, 1982
60. C.J. Glassbrenner, G.A. Slack, Physical Review 134 (4A), A1058-A1069 (1964)
61. E. Yamasue, et al., Journal of Crystal Growth 234, 121-131 (2002)
62. D.F. Gibbons, Physical Review 112 (1), 136-140 (1958)
63. Pankratz, L. B. 1994. Thermodynamic Properties of Carbides, Nitrides, and Other Selected Substances. Bulletin United States Department of Interior, Bureau of Mines.
64. Olesinski, R.W., Kanani, N., and Abbaschian, G.J. 1985. The P-Si (phosphorus-silicon) system. Bulletin of Alloy Phase Diagrams 6 (2), 130-133.
65. Zastrow, U., Houben, L., Meetens, D., Grohe, A., Brammer, T., and Schneiderlochner, E. 2006. Characterization of laser-fired contacts in PERC solar cells: SIMS and TEM analysis applying advanced preparation techniques. Applied Surface Science 252: 7082-7085.